

FOURTH YEAR GROUP INDUSTRIAL PROJECT
UNIVERSITY OF BRISTOL



Experimental development and
validation of a simulated three bar rig
for finite compliance materials testing
Jacob Hutchings, Edward McLaughlin,
Robert Moore and Cui Er Seow

Supervisor:
Dr. M.PEEL

IN PARTIAL FULFILMENT OF THE REQUIREMENTS
FOR THE DEGREE OF
MASTER OF ENGINEERING IN THE SUBJECT OF
MECHANICAL ENGINEERING

April 20, 2016

Acknowledgements

Dr. Matthew Peel for his invaluable experience and guidance in regular meetings throughout the project. *The University of Bristol workshop* who provided the materials, training and equipment to carry out this project. *Dr. Julie Etches* for providing access to the LabVIEW software, digital image correlation equipment and the video extensiometer.

Declaration

The accompanying research project report entitled: "Experimental development and validation of a simulated three bar rig for finite compliance materials testing" is submitted in the fourth year of study towards an application for the degree of Master of Engineering in Mechanical Engineering at the University of Bristol. The report is based upon independent work by the candidates. All contributions from others have been acknowledged above. The supervisors are identified at the start of the report. The views expressed within the report are those of the authors and not of the University of Bristol.

I hereby declare that the above statements are true.

CUI ER SEOW
ROBERT MOORE
JACOB HUTCHINGS

Full Names: EDWARD McLAUGHLIN

Signed (authors): _____

Date: April 20, 2016

Declaration of Copyright

Certification of ownership of the copyright in a dissertation presented as part of and in accordance with the requirements for the Final Degree of Master of Engineering at the University of Bristol, Faculty of Engineering.

I hereby assert that I own exclusive copyright in the item named below. I give permission to the University of Bristol Library to add this item to its stock and to make it available for consultation in the library, and for inter-library lending for use in another library. It may be copied in full or in part for any bona fide library or research worker on the understanding that users are made aware of their obligations under the copyright legislation, i.e. that no quotation and no information derived from it may be published without the authors prior consent.

Authors: CUI ER SEOW
 ROBERT MOORE
 JACOB HUTCHINGS
 EDWARD McLAUGHLIN

Title: Experimental development
 and validation of a simulated
 three bar rig for finite
 compliance materials testing

Date of Submission: April 20, 2016

This dissertation is the property of the University of Bristol Library and may only be used with due regard to the author. Bibliographical references may be noted but no part may be copied for use or quotation in any published work without prior permission of the author. In addition, due acknowledgement for any use must be made.

CUI ER SEOW
ROBERT MOORE
JACOB HUTCHINGS

Full Names: EDWARD McLAUGHLIN

Signed (authors): _____

Date: April 20, 2016

Work allocation

Section						
Edward McLaughlin	Theory and Analysis	Background Theory	Matlab	Stiffness Validation		
Robert Moore				LabVIEW Testing		Report Writing
Cui Er Seow				LabVIEW Testing		
Jacob Hutchings		Matlab		Matlab		
Note: All team members helped out with all areas of the project. This table highlights the main areas each team member worked on.						

Figure 0.1: Work allocation table

Signed:
Edward
McLaughlin:
Robert Moore:
Cui Er Seow:
Jacob Hutchings:

Abstract

This report describes the development and implementation of a feedback control strategy for a tensile test machine, with the aim of simulating a three bar rig that is used to approximate mixed loading conditions. This control strategy is intended to closely approximate the stress state experienced by materials in complex mechanical structures. The method is expected to be particularly useful for testing structures that contain complexities, such as welds, where uncertainty in material properties would challenge more conventional approaches.

The controller is built in LabVIEW and is interfaced with an Instron tensile test machine to simulate three bar rig conditions for varying levels of elastic follow-up on a Compact Tension (C(T)) test specimen. The three bar rig simulations were initially run in the linear-elastic region, followed by extension to the elastic-plastic region to allow the evolution of residual stress to be investigated. The three loading conditions which were analysed are fixed-load, fixed-displacement and finite compliance control. To ensure correct readings, the machine dynamics were characterised and their effects incorporated into the feedback loop.

The results found using the feedback control method have been compared to, and found to be in good agreement with, those produced using a physical three bar rig. This provides evidence for the use of a feedback control method in place of the physical three bar rig. The method also serves as a basis for the use of feedback controllers in mechanical testing to facilitate complex experimental testing.

Contents

Acknowledgements	2
Declaration	2
Declaration of Copyright	3
Work allocation	5
Abstract	6
1 Introduction	13
1.1 Project aims	15
1.2 Report structure	15
2 Literature review	17
2.1 Stress classification	17
2.2 Residual stress	17
2.3 Elastic follow-up	19
2.4 Introducing residual stresses into experiments	20
2.5 Three bar rig	21
2.5.1 Residual stress with the three bar rig	23
3 Algorithm development	26
3.1 Defining the three bar variables	26
3.2 Linear-elastic region	27
3.3 Elastic-plastic region	30
3.3.1 Decoupling crack growth and plasticity	32
3.3.2 Developing residual stress feedback loop in Matlab	33
3.3.3 Matlab results	35
4 Materials and methodology	38
4.1 Aluminium Compact Tension Specimen	38
4.2 Instron Servo-hydraulic test machine	39
4.3 Measuring δ_{CMOD}	40
4.4 Measuring δ_{spec}	40
4.5 Measuring crack length	42
4.6 LabVIEW programming tools	42
4.7 Interfacing with the Instron Test Machine	43
5 Testing measurement accuracy	44
5.1 Decoupling crack growth and plasticity	44
5.2 Validation of stiffness measurements	47
5.2.1 Comparing stiffness and crack length in different failure modes	47

5.2.2	Comparing stiffness measurements with theory	49
5.3	Machine compliance	50
5.3.1	Finding machine displacement	52
5.3.2	Finding $k_{machine}$	53
5.3.3	Validating estimates of machine stiffness	55
5.4	Displacement mapping	56
6	Algorithm implementation and validation	57
6.1	Linear-elastic region	57
6.1.1	Evaluating algorithm behaviour	58
6.1.2	Validating LabVIEW algorithm against manual calculations	59
6.2	Elastic-plastic region	61
6.2.1	Incorporating machine compliance	62
6.2.2	Partial implementation of machine dynamics with a stiffness correction factor	63
6.2.3	Full implementation of machine dynamics	66
6.2.4	Experimental stiffness measurements from partial unloads	71
7	Conclusion	74
8	Future work	75
8.1	Improving methods for finding specimen stiffness	75
8.2	Increasing complexity of loading conditions	75
References		78
A Appendices		i
Appendices		i

List of Figures

0.1	Work allocation table	5
1.1	Explanation of the three loading types	13
1.2	Changing material properties across a simple weld.	15
2.1	Effects of residual stress on "collapse load"	19
2.2	Roche's "Spring Effect" (Roche, 1989)	20
2.3	Photograph of a physical three bar rig (Aird, 2009).	22
2.4	Residual stress relaxation as a result of elastic follow-up	23
2.5	Schematic of the means by which a misfit is applied (Horne, 2013)	23
2.6	Development of residual stress in the three loading conditions	25
3.1	Three bar rig schematic	26
3.2	Matlab results of the three loading conditions in linear-elastic	29
3.3	Linear-elastic data flow loop	30
3.4	Diagram showing decoupling of plasticity and elasticity with unloads	32
3.5	Initial conditions and iterative loop flow chart for the model including residual stress.	34
3.6	Matlab results of the three loading conditions in elastic-plastic region	36
3.7	The effects of load applied to the specimen on residual stress	37
4.1	ASTM Active Standard E399 C(T) specimen geometry	38
4.2	Photograph of machine set-up	39
4.3	Measuring CMOD	40
4.4	Side view of the CT specimen	41
4.5	Front view of the CT specimen	41
4.6	Photograph of Crack length on the face a plastically torn specimen	42
4.7	A schematic of the experimental set-up.	43
5.1	Load-displacement plot demonstrating partial unloads.	44
5.2	Stiffness and plasticity measured from unloads	45
5.3	Using stiffness and plasticity to back-calculate P_{spec}	46
5.4	Comparison of back-calculated P_{spec} to real load	46
5.5	Schematic comparing areas to confirm stiffness	48
5.6	Schematic drawing of machine compliance	50
5.7	Three interpretations of the three bar model	51
5.8	Total vs crack mouth opening displacement	52
5.9	Comparison of machine, specimen and total displacement	53
5.10	Plot of machine displacement with load	54
5.11	Figure comparing specimen, machine and total stiffness	54
5.12	A comparison of specimen stiffness at varying crack lengths	55
6.1	Linear-elastic data flow loop	57
6.2	LabVIEW linear-elastic testing for a constant P_{rig}	59
6.3	Comparison of manual and LabVIEW displacement against load	60
6.4	Comparison of manual and LabVIEW stiffness	61

6.5	Highlight of key steps in the LabVIEW algorithm used in section 6.2.2 and section 6.2.3 on a load-displacement graph.	62
6.6	Data flow loop for the LabVIEW algorithm with the stiffness correction factor.	64
6.7	The experimental results for the relaxation of P_{res} as plasticity increases for the three loading conditions.	65
6.8	LabVIEW elastic-plastic data flow loop with full machine dynamics	66
6.9	Comparison of calculated specimen displacement and measured total displacement	68
6.10	P_{spec} , $P_{applied}$ and P_{res} against displacement	70
6.11	Figure demonstrating the variation in stiffness measured from unloads	71
6.12	The experimental (o) and simulated (\diamond) results for P_{res} for the three loading conditions.	73
8.1	Three bar model with two central bars in series (Smith et al., 2009).	75
8.2	An example of asymmetric loading conditions.	76
A.1	CAD drawing of CT Specimen	i
A.2	Code snippets from the LabVIEW program	ii

List of Tables

1	A table showing the measured crack lengths for of equal elastic stiffness.	48
2	A table showing the contact area for specimens of equal elastic stiffness.	49
3	A table comparing measurements and theoretical calculations of stiffness for different crack lengths.	49

Nomenclature

- α Ratio of outer spring stiffness to specimen stiffness
- $\delta |_{P_{applied}=0}$ Specimen displacement at zero applied load, due to remaining residual displacement plus plastic displacement
- $\delta_{bedding}$ Displacement correction for machine dynamics used to account for the bedding-in effect
- δ_{CMOD} Crack mouth opening displacement
- $\delta_{elastic}$ Elastic deformation of the specimen
- $\delta_{machine}$ Displacement due to compliance in the test machine
- Δ_{misfit} Misfit measured in difference in spring and specimen resting lengths
- $\delta_{plastic}$ Plastic deformation of the specimen
- δ_{res} Displacement of the specimen corresponding to the remaining residual force in the specimen
- $\delta_{res}^{initial}$ Displacement of the specimen corresponding to initial residual force in the specimen
- δ_{rig} Theoretical three bar rig displacement
- δ_{spec} Specimen displacement
- δ_{total} Total displacement of the structure (machine and specimen) as applied by the Instron controller
- a Specimen crack length
- CF Stiffness correction factor
- K Stress intensity factor
- k_{total}^a Combined stiffness of specimen and $k_{machine}^a$
- k_{total}^b Combined stiffness of specimen and $k_{machine}^b$
- K_{IC} Fracture toughness
- $k_{machine}$ Theoretical stiffness of the machine and clevis grips
- $k_{machine}^a$ Machine stiffness during an unload and reload
- $k_{machine}^b$ Machine stiffness on main loading curve (when not performing an unload or reload)
- k_{spec} Stiffness of the specimen

k_{spring}	The combined stiffness of the springs modelled in the outer bars of the three bar rig
k_{total}	Stiffness of entire structure (machine plus specimen)
L	Specimen width (end edge to end edge)
$P_{applied}$	Component of P_{spec} created by applied loading
P_{res}	Component of P_{spec} created by residual loading
P_{rig}	Force applied to the three-bar rig
P_{spec}	Overall load in the specimen
P_{spring}	Overall load in the springs
W	Specimen width (end edge to centre of pinholes)
Z	Elastic follow-up factor
Z_{LL}	Dimensionless specimen compliance
E	Young's Modulus
T	Specimen thickness

1 Introduction

The work presented in this report develops, implements and validates a feedback control strategy that can be used in conjunction with a tensile test machine, to replicate the capabilities of a three bar rig. This will allow investigation into the evolution of residual stress in a small region of a larger compliant structure.

Tensile mechanical testing is commonly used to determine the elastic, plastic, fracture and fatigue properties of a material. Generally, the test machines used during the investigations fall into one of two categories: servo-hydraulic or electro-mechanical. The two types are designed to generate loading through fixed-load or fixed-displacement control respectively.

Fixed-load control is the direct application of load, which can be visualised as an incremental increase in weight that a specimen is directly subjected to, as shown in fig. 1.1 A. The force is generated through equilibrium conditions and is not affected by plastic deformation of the specimen. The specimen is still subjected to the same magnitude of load despite plastic deformation taking place. This means that fixed-load control often leads to unstable failure and plastic collapse once crack growth has initiated (Roche, 1989).

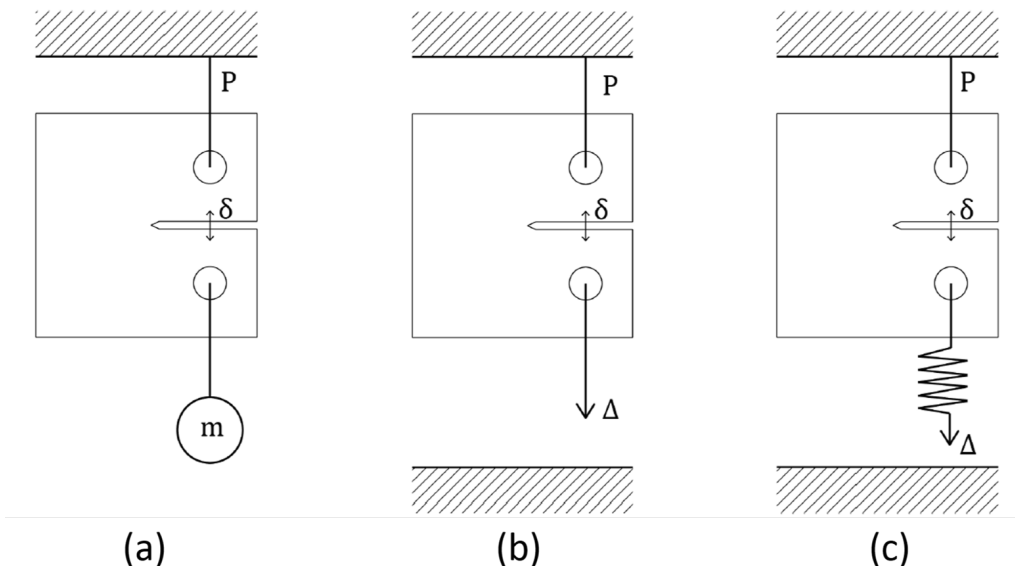


Figure 1.1: (a) Fixed-load boundary condition, (b) fixed-displacement boundary condition, (c) finite compliance applied loading (Seow, 2015)

Fixed-displacement control is the process of inducing a load in a specimen through increasing the geometry that a specimen must comply to, as shown in fig. 1.1(b). Plastic deformation of the specimen acts to reduce the elastic extension required for the specimen to comply to the geometry, hence decreasing the load. This means that fixed-displacement loading generates self-limiting forces, typically leading to stable failure (Roche, 1989).

Until recently many material fracture design principles, such as the R6 methodology (Milne et al., 1988), were solely based on the observation made at the two boundary conditions of fixed-load and fixed-displacement. This has lead to over- or under-conservative designs for those materials subject to loading between the two boundary conditions. While over-engineered

parts will result in higher costs, excess material use and parts being serviced too frequently, under-engineered parts could result in parts failing in industry.

Loading conditions between fixed-load and fixed-displacement are referred to as finite compliance loading conditions due to the condition being induced as a result of compliance in the system. Loading of this type can be represented by a spring in series with a displacement controlled load as shown in fig. 1.1(c), in this scenario the compliance of the spring represents the compliance of the structure (Roche, 1989). Varying the stiffness of the spring from infinitely stiff to infinitely compliant allows the theoretical modelling of both fixed-displacement control and fixed-load control boundary conditions, and also the range in between. Testing between these two boundary conditions is complex and requires the addition of compliance into the system.

The evolution of residual stress in a region of a structure has previously been shown by Horne (2013) to be a function of the loading condition, the level of plastic deformation before failure, magnitude of residual stress, position of applied load. The loading condition is defined by the relative stiffness of the cracked region of a structure compared to the un-cracked region. The influence of the comparative stiffness of a cracked region compared to the stiffness of the outer region is due to a concept called elastic follow-up and will be explored in more detail in the literature review. In the research domain of material failure, it is critical to understand the role of elastic follow-up and its relationship with system compliance and residual stress. This knowledge can be used to create more accurate design codes.

Currently, two main methods have been used to investigate the effect of elastic follow-up and structural compliance: computational non-linear Finite Element Analysis (FEA) (Boyle, 2013), and physical three bar rigs (Aird, 2009). A three bar rig is essentially a physical representation of a finite element model, mimicking a cracked region within an otherwise elastic structure that is uni-axially loaded. Results found using a three bar rig can be used to assess the accuracy of FEA models but can also, in certain circumstances, give more accurate results.

One example where a three bar simulation may be preferable over FEA methods is shown in fig. 1.2 - a plate with a welded joint down the centre. This example is a very simple demonstration of inhomogeneous material properties producing complex material testing scenarios. Illustrative hardness and stiffness profiles through the plate in the x-direction are also shown. The hardness of the plate decreases at the weld due to recrystallisation of the metal, resulting in alignment of grain boundaries. The stress field in the plate increases along the weld due to thermal effects such as differential thermal quenching (Mirzaee-Sisan, 2005). This scenario would be difficult to simulate accurately in FEA due to the unknown material properties. Rather than estimating the material profile in FEA, the structure could be reproduced though replicating the process originally used. Doing so is likely to generate a similar material profile. The replica can then be input into the three bar system to simulate the loading condition that the plate may be subject to in the larger structure.

Previously, as in the work by Aird (2009), investigations using three bar models have been carried out by physically creating a three bar test rig. However, physical three bar rigs have many limitations meaning that investigations are constrained and time consuming. For this reason the ability to develop a feedback controller that allows fixed-displacement controlled test machines

to investigate the finite compliance region is useful.

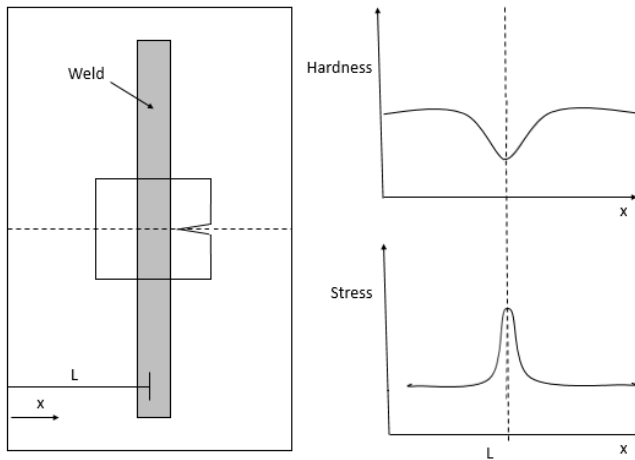


Figure 1.2: Changing material properties across a simple weld.

1.1 Project aims

The overall aim of the project is to create a feedback controller modelling a three bar rig, which can be used together with a tensile test machine to apply finite compliance loading conditions to a compact tension C(T) specimen in the elastic and plastic region. This overall aim can be broken down into five individual requirements:

- simulate the three bar rig in the elastic region with the inclusion of elastic follow-up
- simulate the three bar rig in the elastic-plastic region, accounting for the effects of plasticity on residual stress
- accurately decouple crack growth from plastic deformation, using partial unloads to examine the current specimen state
- investigate and model the compliance of the test machine incorporating the necessary corrections in to the control algorithm to ensure accurate results
- implement and validate the simulated models using LabVIEW programmes as a controller that interfaces with the tensile test machine.

1.2 Report structure

So far the subject of the report, its aims and its purpose have all been discussed in section 1. Section 2 reviews previous literature outlining the main engineering principles and eminent work in this research area. The development of the algorithms used to model the three bar rig are laid out in section 3. The methodology, materials and testing procedures are discussed in section 4. The accuracy of the testing measurements are examined in section 5 in order to incorporate phenomena such as machine compliance into the algorithms. Section 6 presents and discusses

the results from the mechanical testing, evaluating the algorithms representation of a three bar rig. Concluding remarks and ideas for future work are contemplated in sections 7 and 8.

2 Literature review

In this literature review, the concepts of elastic follow-up and residual stress are discussed, as well as their relationship with stress classification. The codependency of these three concepts becomes apparent and thus the need to proceed through this project with them all in mind is evident. The purpose of the three bar rig and its experimental effectiveness is also examined.

2.1 Stress classification

Roche (1987) examined the distinction between primary and secondary stresses in the elastic plastic region, assessing the varying amounts of elastic follow-up (explained in section 2.3). The impact of elastic follow-up was examined through the effects of primary and secondary stresses on crack behaviour. It is argued, with reference to thin walled pressure vessels, that the industry wide “design by rules” strategy of comparing stress states with material constants (e.g. yield strength, fracture toughness) leads to overly conservative design, resulting in more expensive solutions. It is also stated that the finite elements methods of design are not “efficient”, particularly with respect to categorising the stresses. It is not always clear which category a stress belongs to and so the decision can often require engineering judgement. A solution of “design by analysis” is proposed, in which stresses are categorised into primary and secondary stresses, the effects of which are assessed using limit analysis.

(Roche, 1989) built on these concepts in the context of nuclear component design by justifying the use of limit analysis in conjunction with stress classification for effective design. Formal definitions are presented, as given in the nuclear component design codes, for primary and secondary stresses. Primary stresses are defined as applied loads which maintain a force equilibrium between the structure and the environment. These stresses cannot disappear due to plasticity within the material, and so are not self-limiting. Secondary stresses, on the other hand, are self-limiting and are produced by self-constraint or constraint from surrounding material. These forces may disappear as a result of creep or plasticity. Neither an applied load nor a residual load results in a purely primary or a purely secondary stress. A purely primary or purely secondary stress is never apparent in the real world.

2.2 Residual stress

Residual stresses are most often introduced during manufacturing processes where welding or thermal cooling results in differential temperature gradients, or through misfits in assemblies. These processes produce internal stresses between regions of a material as they attempt to expand or contract against each other. Withers and Bhadeshia (2001) explained how a residual stress, as a secondary stress, is not necessary to maintain a force equilibrium between a material sample and its environment. While it was stated that residual stresses may be categorised in various ways (e.g. means of measurement, thermal or misfit), Withers and Bhadeshia (2001) categorised them by length scale; type I (macro-scale), type II (grain scale) and type III (atomic scale). While type II and III residual stresses are almost always apparent due to manufacturing processes or multiphase grain properties in alloys, over a large enough volume V_0 , these stresses

average out. Similarly, as soon as volumes larger than V_0 are considered (e.g. drilling holes), residual stresses over these length scales are negligible. Thus, it is only for length scales which correspond to volumes less than V_0 that type II and type III (for their respective V_{0II} and V_{0III}) residual stresses should be a consideration.

Green and Knowles (1994) sub-categorises type I (macro-scale) residual stresses into short-, medium- and long-range secondary stresses and defines their effects on crack growth in pressure vessels. The given range of a residual stress will have a varying effect on a structure as it will be self-limiting or not over different length scales, with longer range residual stresses self-limiting over longer distances. Stress concentration factors were examined for the three different ranges of secondary stresses in the case of through-thickness cracks. Thin-walled, closed-ended pressures vessels were tested with internal pressures and bending moments. It was found that the longer the range of the secondary stress the higher the correlation between crack length and stress intensity factor. Furthermore, in general, stress intensity factor was shown to increase with crack length to a limiting value. On the basis of these findings, extra stress contribution can be encompassed into conventional calculations for yielding and global failure of pressure vessels, with particular reference to leak-before-break design.

From Green and Knowles (1994), Aird (2009) concludes with the following statement:

"This suggests that, depending on the level of elastic follow-up, long-range residual stresses may provide a significant contribution to the plastic collapse of a structure, whereas short and medium-range stresses will not. Finally, although elastic follow-up effects may have a significant impact on the integrity of a cracked structure, the Green and Knowles stress classification scheme does not take elastic follow-up into account. This means that, for the purpose of structural integrity calculations, further classification is necessary in order to account for elastic follow-up."

That is to say that while Green and Knowles (1994) classifies long-range type I residual stresses to be the primary concern for plastic collapse, the effects of elastic follow-up on these stresses could have a further implication on material failure. This is something which is largely unaccounted for by Green and Knowles (1994) and could result in medium range type I residual stresses also having an effect on plastic collapse. Furthermore, it is also worth noting that Green and Knowles (1994) categorised the different ranges of type I stress (short-, medium- and long-range) by their effects on the material and not by a quantitative range of length scales. This leads to categorisation after the stresses have already affected the material in question which is not useful for industrial design purposes.

Smith et al. (2009) noted that residual stresses are usually considered to be secondary stresses, however, if the residual stresses are long-range (i.e. self-equilibrate over long distances) then they will not balance across a small cracked area. Under these conditions residual stresses may be considered at primary stresses on the cracked region and can have a serious effect on material failure.

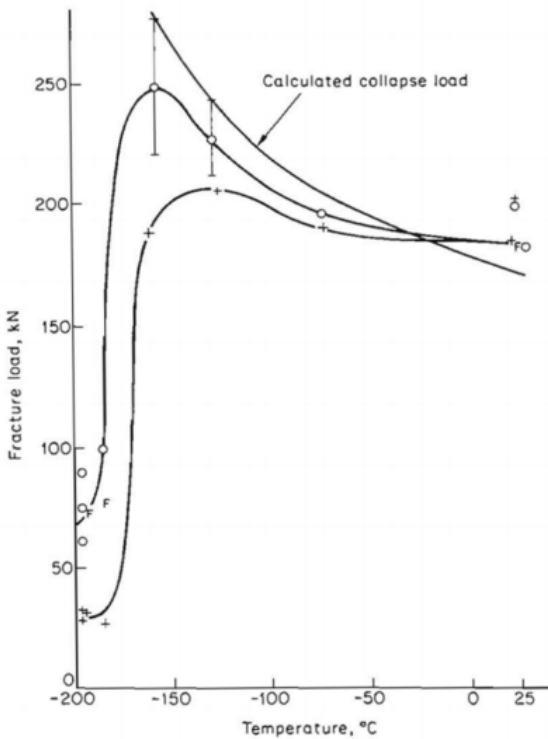


Figure 2.1: Effects of residual stress on "collapse load" from Chell (1979): fracture loads as a function of temperature for specimens with (+) and without (o) residual stresses. (F) represents fatigue pre-cracked specimens without residual stress.

Chell (1979) demonstrated how Residual and Thermal (RT) stresses can affect the failure modes, and points of failure of structures. The effects of RT stresses are summarised to significantly reduce the load bearing capacity of a structure (fig. 2.1) and as the structure approaches plastic collapse the residual stresses relax so that the load on the specimen is dominated by the mechanical applied load. It is noted that while secondary stresses such as RT stresses are self-equilibrated within the entire structure, they may not be in a given substructure. In this case, the secondary stresses act as primary stresses on the substructure and will affect its plastic collapse (in agreement with Smith et al. (2009)). Hence, design practices must take into account the effects of secondary stresses on plastic failure with reference to elastic follow-up. To demonstrate this, the example of a tensile test machine and a specimen with a fatigued notch was taken.

2.3 Elastic follow-up

Reviewing the literature, elastic follow-up can be defined as the effect of surrounding material on the rate of relaxation of a deforming non-linear region. If structural design is made assuming perfect (fixed-displacement control) or no (fixed-load control) elastic follow-up is in the system, it will lead to under- or over-engineered parts respectively. Depending on the amount of elastic follow-up, a stress will be either predominantly fixed-load (purely primary), predominantly fixed-displacement (purely secondary) or somewhere in between. The rate of relaxation of

secondary stresses, such as residual stresses, is largely dependent on the type of applied stress on the structure – fixed-load, fixed-displacement or finite compliance loading. Thus elastic follow-up governs the rate of relaxation of residual stresses. Elastic follow-up was first considered in Robinson and Schenectady (1955) under the name of “follow-up elasticity” in an investigation of creep concentrations in steam piping design. In this paper, it is found that the relaxation time of secondary stresses is dependant on both material properties and the amount of follow-up elasticity in the system.

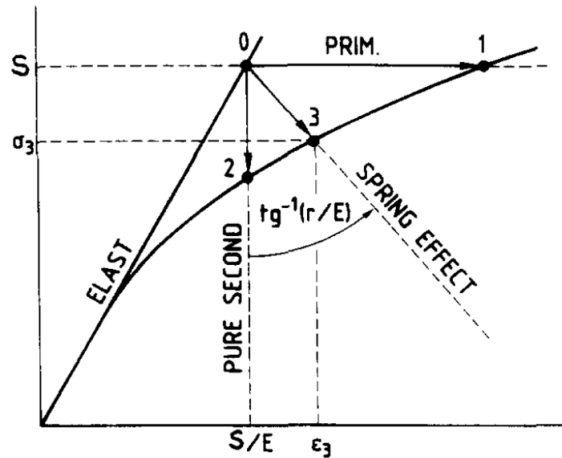


Figure 2.2: Roche's "Spring Effect" (Roche, 1989)

Roche (1989) examined the effect of elastic follow-up on stress classification through the idea of a 'spring effect'. While loading in either fixed-load (pure primary) or fixed-displacement (pure secondary) stresses will result in following either path 1 or 2 (as labelled in fig. 2.2), loading in finite compliance control will lead to taking path 3. Defining the amount of elastic follow-up as the gradient of path 3 from vertically down, anti-clockwise, fixed-load has a gradient of 0 while fixed-displacement has an infinite gradient, thus the degree to which a stress is primary or secondary is characterised by the gradient of this line, and therefore, the amount of elastic follow-up.

Now that the concept of elastic follow-up has been introduced, the reason for stresses never being purely primary or purely secondary may be explained. This fact is well presented by Bazant and Becq-Giraudon (1999). In their paper, the effects of the ductility on the fracture mechanics of a substructure are examined. The levels of ductility in the structure govern its ability to resist overload by redistributing internal loads. Specifically, the ductility of material surrounding a smaller substructure, which will always be finite, creates elastic follow-up across the substructure. This means that neither loading condition, fixed-load or fixed-displacement, may occur on the substructure - only finite compliance loading.

2.4 Introducing residual stresses into experiments

In order to look at the effect of elastic follow-up on the rate of relaxation of residual stresses, a precise and repeatable means to introduce residual stresses into an experiment is required. A brief overview of a non-exhaustive list of controlled methods to introduce residual stresses

into test specimens is discussed in this section. As well as introducing residual stresses, these methods are likely to produce inhomogeneous material properties which affects failure modes and material behaviour. Firstly, mechanical methods will be discussed followed by thermal and welding.

While mechanical methods such as the application of in-plane compressive and tensile stresses exist, the method of Local Compression (LC) or side punching into materials is focused on in this literature review. Meith et al. (2003) find that applied LC around the crack results in a lower fracture toughness. It was also shown that the reduction in fracture toughness is largely independent of the amount of LC whereas the location of the compression is important. The closer to the front face it is located the less the effect is on the fracture toughness. A concurring view on LC location relative to the crack was found in Mahmoudi et al. (2003). In their paper both single and double punch techniques are used and compared to Finite Element (FE) results from ABAQUS software. It was also found that the diameter of the punching tool had an effect on the reduction in fracture toughness. Ogeman (1993) used stress coining to create tangential LC stresses on the bore of a hole and compared the results with FE methods. While the FE results were in good agreement with the experimental results, in that the crack propagation can be up to an order of magnitude less having applied the stress coining, the relaxation of the induced residual stress is not taken into consideration as the crack grows. Hadidi-Moud et al. (2003) further emphasises the need to understand the effects of residual stress on failure modes through exploring its effect on cleavage fracture toughness. Residual stresses are again introduced using LC techniques. Their paper is in good agreement with Meith et al. (2003) and Mahmoudi et al. (2003) that the compressive residual stresses generated by LC cause a reduction in fracture toughness.

Residual stresses from thermal quenching are introduced due to differential thermal contraction. The extent of this has been shown in square section bars has been investigated in Mirzaee-Sisan (2005). It is asserted that the residual stresses only remain apparent at room temperature if there is plastic deformation while the material is held at a high temperature. The extent and distribution of these residual stresses are accurately modelled in Simsir and Gur (2008) using a 3D FEM model, thermal histories and micro-structure evolution. Similar effects of thermal contraction occur during welding, resulting in a tensile residual stresses in the welded material and a balancing compressive residual stress in the surrounding material.

A fourth method of introducing residual stresses is to implement a misfit within a three bar rig. The three bar rig is discussed in detail in section 2.5. This is the method which this project models.

2.5 Three bar rig

In this project, the example of the three bar rig will be used as a test scenario for the feedback system. In recent years, the idea of a three bar rig has been developed to further understand the co-dependency of stress classification, residual stress and elastic follow-up and their implications on one another. This section will go into detail on the principles of the three bar rig and look at notable work demonstrating the relationships between stress classification, residual stress

and elastic follow-up. This will act as a basis for the project undertaken – the development of a simulated three bar rig.

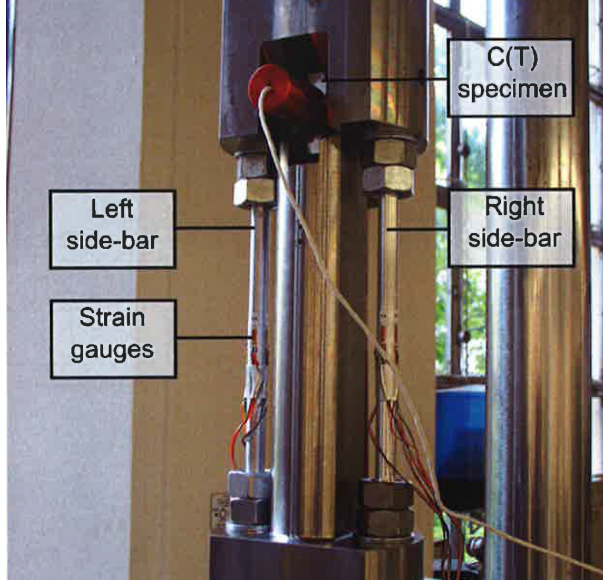


Figure 2.3: Photograph of a physical three bar rig (Aird, 2009).

In this project we will use the example of the three bar rig as a test scenario for the feedback system. The three bar model is shown in fig. 3.1. The utility of this model is discussed extensively in Aird (2009) and Horne (2013). In Aird (2009), a physical three bar rig is used as shown in fig. 2.3. The development of residual stresses as applied load is increased has been successfully demonstrated for the three loading conditions; load control, displacement control and finite compliance loading. These are shown graphically in fig. 2.6. It is shown that in load control (very low values of alpha as defined by eq. 3.1), the residual stress stays constant. As alpha increases i.e. the central bar is stiffer relative to the outer bars, the residual stress diminishes as a load is applied.

While the three bar model is a good aid to represent elastic follow-up and residual stresses, through varying the relative bar stiffness and implementing misfits respectively, it has short comings. The compliance is limited by the stiffness ratio of the outer and inner bars. The maximum displacement of the test is limited to the extensions within the linear-elastic region of the outer bars and the maximum sweep of the machine.

Smith et al. (2009) examines multi-bar systems, including a three bar rig, to look at how elastic follow-up is related to the relaxation of residual stress. It is shown that just as there is a relationship between elastic follow-up and the introduction of residual stress through a misfit of bars in series, there is a relationship between the relaxation of the residual stress and elastic follow-up. The relative stiffness of the outer bars to the inner bars is given by:

$$\alpha = \frac{nk_{outer}}{k_{inner}} \quad (2.1)$$

The paper begins with a three bar model analysis and then extends it to multiple outer bars

and also an array or bars in series and parallel arrangements. It is shown that the theory of a three bar model is extendible to multi-bar models. Fig. 2.4 shows in blue the load-displacement for the central bar and in red the load-displacement for the outer bars. Points A and B are the residual stresses for the two bars as a result of a misfit. It is shown that the gradient of the line A to C is inversely related to the elastic follow-up (relative stiffness) of the system. Thus the rate of relaxation of the residual stress is inversely proportional to elastic follow-up.

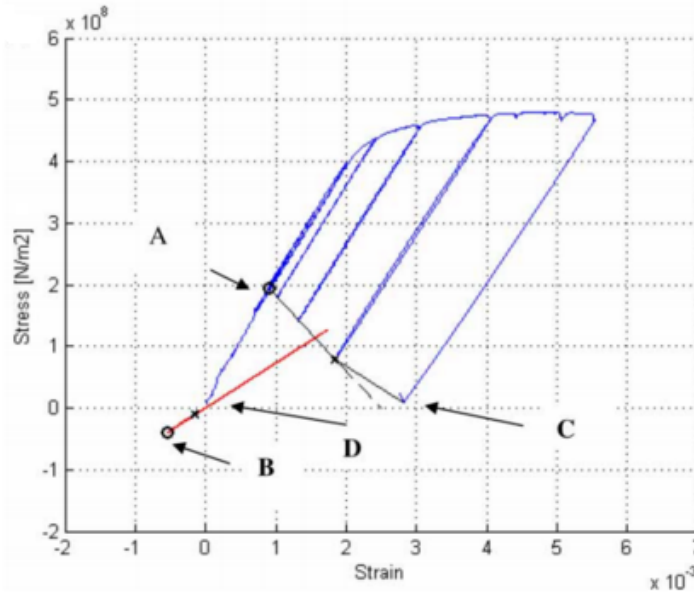


Figure 2.4: Residual stress relaxation as a result of elastic follow-up from Smith et al. (2009). Points B and D and the line on which they are situated refer to the outer bars while points A and C and the line on which they are situated refer to the central bar.

A definition of α has already been given as the stiffness ratio of the outer bars to central bar in a multi-element model (eq. 2.1). A summary of the mathematical model of the three bar rig developed and used by Aird (2009); Smith et al. (2009); Horne (2013) will now be presented.

2.5.1 Residual stress with the three bar rig

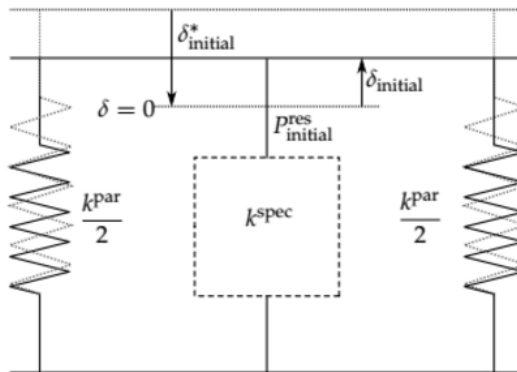


Figure 2.5: Schematic of the means by which a misfit is applied (Horne, 2013)

As well as modelling elastic follow-up, residual stresses may be modelled by using a three bar model. The mathematical modelling presented in this section follows the process taken by Horne (2013), similar approaches are made by Aird (2009); Smith et al. (2009). This is done through implementing a misfit between the outer springs and the central spring. Any residual stress introduced through a misfit will produce equal and opposite forces in the central and outer springs.

$$P^{res} = k^{spec} \delta^{spec} = -k^{par} \delta^{par} \quad (2.2)$$

The initial displacement on the specimen due to the misfit, as shown in fig. 2.5, is given by:

$$\delta^* = \delta^{par} - \delta^{spec} \quad (2.3)$$

where δ^* is the size of the misfit and δ^{spec} and δ^{par} are the displacements of the springs and specimen from a common reference point. Substituting eq. 2.3 into eq. 2.2:

$$k^{spec} \delta^{spec} = -k^{par} (\delta^* + \delta^{spec}) \quad (2.4)$$

$$\delta^{spec} = -\frac{k^{par}}{k^{par} + k^{spec}} \delta^* \quad (2.5)$$

letting δ_{spec} be replaced as $\delta_{res}^{initial}$ and substituting $\alpha = \frac{k_{spring}}{k_{spec}}$:

$$\delta^{res} = -\frac{\alpha}{\alpha + 1} \delta^* \quad (2.6)$$

$$\delta_{res} = \frac{\alpha_{eff}}{\alpha_{eff} + 1} \delta_0 \quad (2.7)$$

where n is the number of outer bars and eqs. 2.6 and 2.7 use the notation directly from Horne (2013) and Smith et al. (2009) respectively. The change in sign is due to the convention taken for positive direction of displacements. The force in the specimen due to the residual stress and its rate of change with respect to stiffness is then calculated by Aird (2009); Horne (2013) to investigate the behaviour of the residual stress as specimen stiffness, and hence, α changes.

$$P^{res} = -k^{spec} \frac{\alpha}{\alpha + 1} \delta^* \quad (2.8)$$

where $\delta^* = \delta_{initial}^* + \delta^{pl}$ Defining ψ as the rate of change of P^{res} with respect to specimen stiffness, k_{spec} .

$$\psi = \frac{\partial P^{res}}{\partial k^{spec}} = -\left(\frac{\alpha}{\alpha+1}\right)^2 \delta^* \quad (2.9)$$

From eq. 2.9 the behaviour of the residual stress in fixed-load ($\alpha \rightarrow 0$) and fixed-displacement ($\alpha \rightarrow \infty$) control are examined. In fixed-load control:

$$\alpha \rightarrow 0; \frac{\alpha}{\alpha+1} \rightarrow 0 \quad (2.10a)$$

$$\psi|_{\alpha \rightarrow 0} \rightarrow 0 \quad (2.10b)$$

therefore, residual stress is shown by Horne (2013) to be constant in fixed-load control. In fixed-displacement control:

$$\alpha \rightarrow \infty; \frac{\alpha}{\alpha+1} \rightarrow 1 \quad (2.11a)$$

$$\psi|_{\alpha \rightarrow \infty} \rightarrow -\delta^* \quad (2.11b)$$

therefore, residual stress is shown by Horne (2013) to diminish with plasticity in fixed-displacement control. These results are shown graphically by Aird (2009) in fig. 2.6.

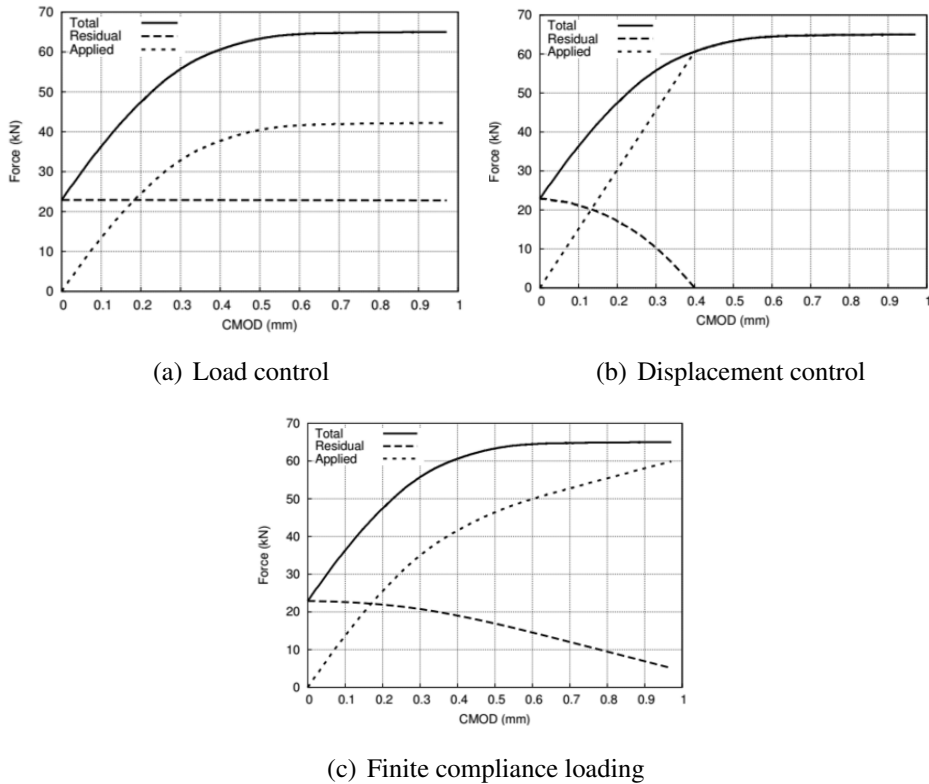


Figure 2.6: The development of residual stress in the three loading conditions (Aird, 2009), CMOD is the crack mouth opening displacement of a C(T) specimen.

3 Algorithm development

To develop a feedback control system a deep understanding of the physical three bar rig and its representation as a mathematical model is required. Following on from previous work reviewed in the literature, this section provides an in depth breakdown of the mathematical model used in the algorithm and the capabilities of the three bar system. The algorithm shall be initially developed using Matlab as a modelling platform before being transferred to LabVIEW.

3.1 Defining the three bar variables

A physical three bar rig is used to approximate a sub-structural element, containing a crack, surrounded by some larger scale structure. As previously shown in fig. 2.3, the physical rig is comprised of two outer bars that represent the elastic region of the structure and a compact tension (C(T)) specimen that represents the cracked, non-linearly deforming region. For the three bar rig to be effective, the outer bars must remain within their elastic region, therefore, the system can be conceptually represented by two springs in parallel with a central specimen. This mathematical model is illustrated in fig. 3.1.

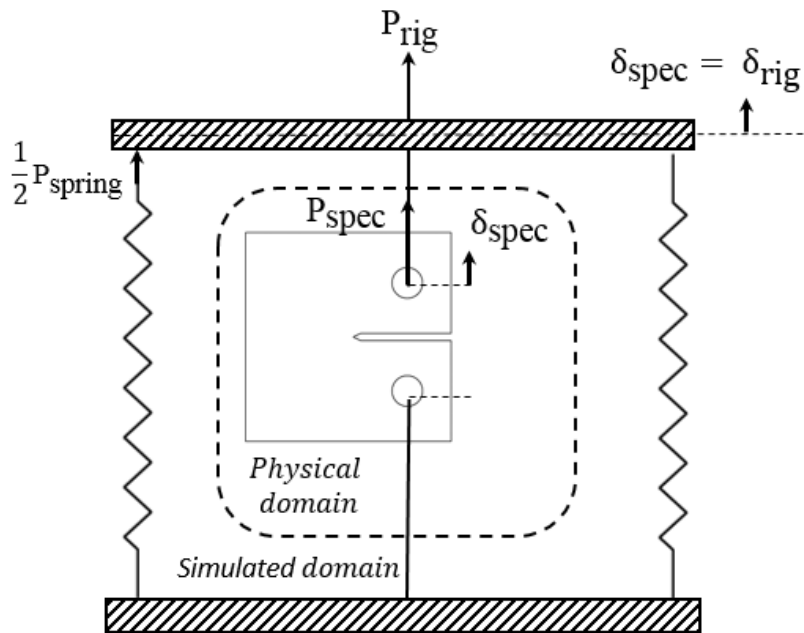


Figure 3.1: Three bar rig schematic

To develop a controller, the model must be split into two domains: the physical specimen that is subjected to tensile loading and the simulated three bar set-up. As the control method aims to remove the need for a physical rig, only the specimen is present in the test machine. The loading condition that the specimen is subjected to is dependent on the properties of the simulated outer bars. The simulation of the outer bars gives added capabilities to the control feedback three bar rig over its physical counterpart.

Physical rigs are limited to a range of displacement and stiffness ratio inputs. This is

because the physical outer bars are limited to displacements within their elastic region and to practically applicable stiffness values. Simulating the outer bars, as the control feedback method does, allows any displacement and any stiffness ratio to be applied. Physical rigs also have to manufactured to a given initial stiffness ratio meaning a new rig must be produced each time a new stiffness ratio is to be investigated. In contrast, the feedback controller is more adjustable as a simple mathematical change to the k_{spring} input, replaces the need to produce a new rig.

The three bar rig is subjected to a displacement δ_{rig} which is equal in magnitude to the displacement of the specimen, δ_{spec} . This displacement in turn produces a force in the specimen, P_{spec} . Due to the parallel set-up, the displacement of the specimen must be equal to that of the outer springs δ_{spring} , thus creating a load in the spring, P_{spring} . The corresponding force on the rig, P_{rig} , is a summation of the load in the springs and the loads in the outer bars.

The distribution of P_{rig} between the specimen and the outer springs is determined by their relative stiffness. The ratio between the stiffness of the specimen and that of the bar, α , is defined by:

$$\alpha = \frac{k_{spring}}{k_{spec}} \quad (3.1)$$

where k_{spring} is the combined stiffness of the two springs, and k_{spec} is the stiffness of the specimen.

In this report, $\alpha = 1 \times 10^9$ and $\alpha = 1 \times 10^{-9}$ has been used to define fixed-displacement control and fixed-load control respectively.

3.2 Linear-elastic region

Within the elastic region, the load distribution is only dependent on the relative stiffness of the specimen and outer springs in accordance with Hooke's law. P_{rig} is given by:

$$P_{rig} = (k_{spec} + k_{spring})\delta_{spec} \quad (3.2)$$

therefore, δ_{spec} and P_{spec} are given by:

$$\delta_{spec} = \frac{P_{rig}}{k_{spec} + k_{spring}} \quad (3.3)$$

$$P_{spec} = k_{spec}\delta_{spec} = \frac{P_{rig}}{1 + \alpha} \quad (3.4)$$

The stiffness of the a compact tension specimen C(T) as used in this study, k_{spec} , can be calculated (Anderson, 2005):

$$k_{spec} = \frac{TE}{Z_{LL}} \quad (3.5)$$

where T is the specimen thickness (as shown in fig. 4.1), E is the Young's Modulus of the material that the specimen is made from and Z_{LL} is the non-dimensional compliance. Z_{LL} is determined by the specimen geometry thus it is a function of crack length a and width W (as shown in fig. 4.1).

$$Z_{LL} = \left(\frac{1 + \frac{a}{W}}{1 - \frac{a}{W}} \right)^2 \left[2.163 + 12.219 \left(\frac{a}{W} \right) - 20.065 \left(\frac{a}{W} \right)^2 - 0.9925 \left(\frac{a}{W} \right)^3 + 20.609 \left(\frac{a}{W} \right)^4 - 9.9314 \left(\frac{a}{W} \right)^5 \right] \quad (3.6)$$

As crack length increases in the specimen, the ratio of crack length to specimen width, a/W , becomes larger, increasing the non-dimensional compliance of the specimen and decreasing its stiffness, k_{spec} . The reduction in k_{spec} means that the load for a given δ_{rig} will decrease, however the size of the reduction is dependent on the initial value of α .

As described in the literature review, a very high initial value of α (i.e. $\alpha = 1 \times 10^9$) approximates fixed-displacement control, where the springs are infinitely more stiff than the specimen. The stiffer springs bear the majority of P_{rig} . Conversely, a very low initial value of α (i.e. $\alpha = 1 \times 10^{-9}$) approximates fixed-load control, where the springs are infinitely more compliant than the specimen. The stiffer specimen bears the majority of the P_{rig} .

Varying α between the extreme values of fixed-load and fixed-displacement allows finite compliance loading conditions to be applied. As compliance of the outer bars increases, the magnitude of load shedding from the specimen to the outer bars decreases. The amount of elastic follow-up that takes place is defined by the the elastic follow-up factor, Z , which is a function of the stiffness ratio between the specimen and the outer bars (Smith and Hadidi-Moud, 2011):

$$Z = \frac{\alpha + 1}{\alpha} \quad (3.7)$$

thus, in fixed-load control, $Z \rightarrow \infty$, and in fixed-displacement control, $Z \rightarrow 1$. Increasing the compliance in the outer bars increases the level of elastic follow-up.

To summarise, the three bar rig approximates the behaviour of a non-linear deforming substructure in a larger elastic region. Mathematical equations can be used to model the stiffness of the outer region, adding compliance into the structure. Varying the ratio of stiffness of the outer bars in relation to the specimen changes the level of elastic follow-up and affects the evolution of stress in the system.

To investigate the effect of different stiffness ratios and crack growth on the evolution of load in a three bar rig, a Matlab simulation was used. The Matlab code was designed to operate in an iterative manner that represents the way in which the final controller will interact with the test machine. The model is split into two distinct sections; a numerical model of the three bar rig and a model of theoretical specimen behaviour. The former simulates the conditions of the three-bar rig on the specimen; the latter models elastic specimen behaviour using Hooke's law. The latter model will later be replaced by feedback from a test machine. A Matlab simulation

Developing the controller to accurately reproduce known three bar phenomena in the elastic region is a logical first step that provides solid grounding for later work.

An example of the behaviour of this model is shown in fig. 3.2. Firstly, a $P_{initial}^{spec}$ of 12 kN was selected, then the required displacement to produce $P_{initial}^{spec}$ was calculated using a theoretical k_{spec} . The corresponding $P_{rig}^{initial}$ was then calculated, based on the initial spring and specimen stiffness, using eq. 3.2. From this point onwards P_{rig} was held at this value. Once loaded, a/W was increased to represent crack growth. The crack growth causes the stiffness of the specimen to fall, altering the stiffness ratio, α . Depending on the initial α value for the simulation, the effect of a/W increasing sheds the load from the specimen to the outer bars in varying degrees.

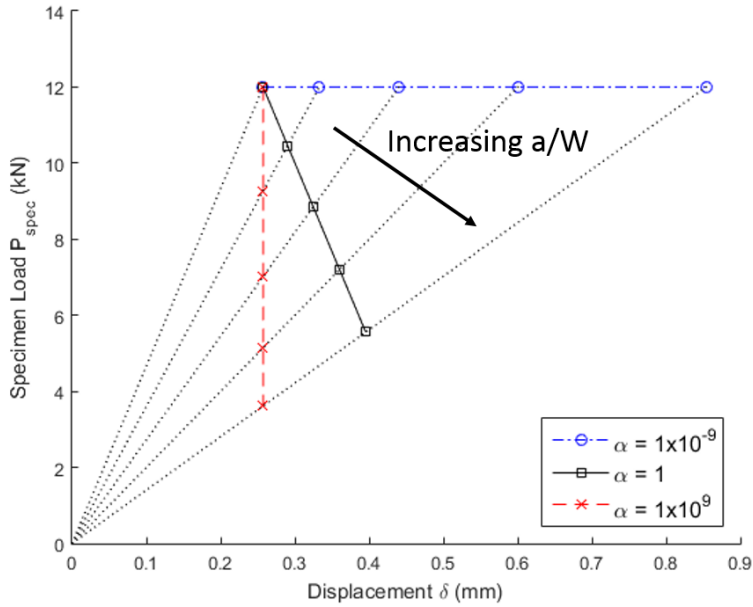


Figure 3.2: Matlab results showing the change in load with crack growth for three initial α values within elastic region. The dashed lines display loading lines for different a/W , indicating equal crack length on each load condition.

In fixed-displacement control ($\alpha = 1 \times 10^9$), as a crack develops (i.e. a/W increases), the reduction in the net cross-sectional area decreases the stiffness of the specimen which causes α to increase. This change in α redistributes the load to the springs, therefore, as α increases the share of P_{rig} that the specimen is subjected to reduces, while the displacement of the specimen remains constant. This effect can be seen in fig. 3.2,

Conversely, in fixed-load control ($\alpha = 1 \times 10^{-9}$), as a crack develops, the changing specimen stiffness has very little effect on an already infinitely small stiffness ratio. The outer springs are very compliant in comparison to the specimen thus they retain very little of the load. Therefore, as crack growth occurs, P_{spec} remains approximately equal to P_{rig} as specimen displacement increases.

For values of α in between the two loading conditions, the force on the rig is shared between the specimen and the springs, and the effect of the decrease in specimen stiffness as a crack develops is in accordance with their stiffness ratio. This results in specimen behaviour in between that of the other two extremes, with load decreasing and specimen displacement increasing, as

seen in fig. 3.2.

To further develop the Matlab code so that it represents a feasible experimental test, a method to maintain the initial P_{rig} needs to be defined. In real testing, crack growth will be extended through fatigue cycling. The decrease in stiffness of the specimen, due to crack growth, reduces the overall stiffness of the three bar rig, which reduces P_{rig} . To increase P_{rig} back to the initial P_{rig} , δ_{spec} must be increased to a new displacement, δ_{eq} . δ_{eq} is the displacement required for $P_{rig} = P_{rig}^{initial}$. Once loaded back to δ_{eq} , crack growth can be further propagated. These additional steps are shown in a full data loop in 3.3. This data loop forms the basis on which the implemented LabVIEW code is built.

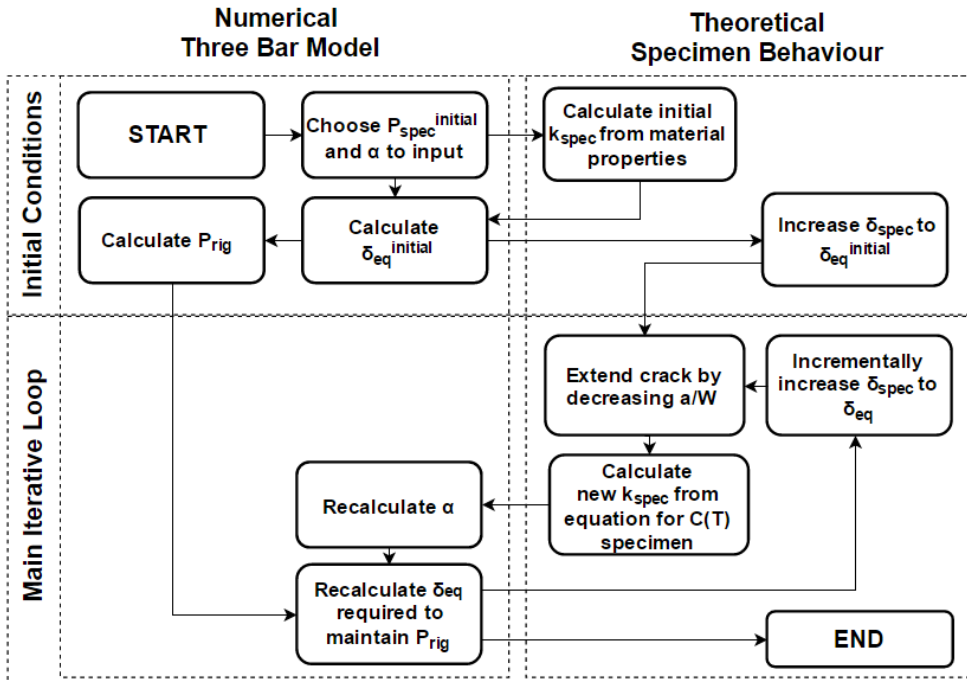


Figure 3.3: Linear-elastic data flow loop

This simulation furthered understanding of the three bar rig, confirmed the mathematical model and aided in the development of the iterative control loop. In the next section, model will be further developed to incorporate the effects of plasticity and to implement residual stress on the specimen.

3.3 Elastic-plastic region

As discussed in the introduction, the main objective of the three bar rig is to allow investigations into the evolution of residual stress. The initial elastic model demonstrates that the three bar model successfully implements finite compliance loading conditions, but it does not yet include residual stress or the effects of plasticity. In this section the equations which incorporate these effects into the LabVIEW algorithm will be explained.

A key difference between the physical three bar rig and the simulated version is how the residual stress is applied. In the physical rig, the residual stress is applied through tightening bolts which attach the outer bars to the three bar rig, and the applied stress is exerted using the load exerted by the tensile test machine. However, without a physical rig the only way to exert both the residual and applied force on the specimen is by using a tensile test machine i.e. there is one means to apply two distinct forces. Hence, the force exerted by the tensile test machine is a superposition of the applied and residual force experienced by the specimen. It is therefore logical, for simulation purposes, to define P_{spec} as a summation of the specimen load due to the residual stress P_{res} , and specimen load due to the applied force, $P_{Applied}$. An equation is required to simulate residual stress for a given Δ_{misfit} , which would otherwise result naturally from the tightened bolts, as would occur in a physical rig.

As shown previously in the literature review, there is a strong relationship between the level of elastic follow-up and the rate of relaxation of residual stress. A residual stress is introduced that is self-limiting over the entire three bar rig (springs and specimen). However, while the stress is self-limiting over the entire rig, it is not necessarily self-limiting over the specimen. The stress borne by the specimen will, therefore, be partially a primary stress and partially a secondary stress, the ratio of which is dependant on the value of α . For high values of α , i.e. fixed-displacement control, the stress is predominantly secondary, conversely, for low values of α , i.e. fixed-load control, the stress is predominantly primary. The effects of these conditions on the evolution of residual stress are examined in this section.

Consider the spring-specimen set-up in fig. 2.5. The natural state of the system is shown on the left, where the springs and specimen have a height difference given by Δ_{misfit} . The top bar is then attached to the specimen, causing the springs to compress by $(\Delta_{misfit} - \delta_{res})$, and the specimen to extend by δ_{res} . The ratio of the spring compression and the specimen extension is dependent on the initial value of α . The misfit creates a residual load which acts in tension on the specimen. Initially, considering the linear-elastic behaviour only, from the vertical force balance, the tensile P_{res} in the specimen must be equal to the compressive force, P_{spring} , in the springs.

$$P_{res} = -P_{spring} \quad (3.8a)$$

$$k_{spec}\delta_{res} = k_{spring}(\Delta_{misfit} - \delta_{res}) \quad (3.8b)$$

Rearranging in terms of α and factorising δ_{res} gives:

$$\delta_{res} = \frac{\alpha}{(1 + \alpha)}\Delta_{misfit} \quad (3.9)$$

plastic deformation of the specimen, $\delta_{plastic}$, acts to counteract the height of this misfit. Hence, it is included as a term which is subtracted from Δ_{misfit} , which gives:

$$\delta_{res} = \frac{\alpha}{(1 + \alpha)}(\Delta_{misfit} - \delta_{pl}) \quad (3.10)$$

from this, the residual force acting on the specimen P_{res} can be found from:

$$P_{res} = k_{spec} \delta_{res} \quad (3.11)$$

By substituting values for Δ_{misfit} , α , k_{spec} and $\delta_{plastic}$ at any point, the remaining residual load, P_{res} may be found using eqs. (3.10) and (3.11). However, a partial unload is required to determine k_{spec} and δ_{pl} at any given point on the elastic-plastic curve.

3.3.1 Decoupling crack growth and plasticity

While a specimen is in a loaded state, it is not possible to decouple the level of plasticity from the current stiffness if only the displacement and load are known. Both specimen stiffness and plasticity are required to properly model the behaviour of the three bar rig.

During loading microscopic plasticity is always apparent at the crack tip, however, macroscopic plasticity only occurs when the material is loaded past its yield point. This macroscopic plasticity takes place in the elastic-plastic region. In this region of material testing, both elastic extension, $\delta_{elastic}$, and plasticity, $\delta_{plastic}$ contribute to the total extension of the component.

$$\delta_{spec} = \delta_{pl} + \delta_{elastic} \quad (3.12)$$

The stiffness of the specimen, and hence the crack length, can be measured from the gradient of the partial unload while x-intercept of the unload gives a value for plastic deformation. As will be seen from the fixed-load control experimental results in fig. 6.2b, when unaccounted for, plasticity effects will cause the controller to deviate from theoretical predictions. Thus, the three bar rig controller must be extended to incorporate plasticity effects if the specimen is to be loaded into the plastic region.

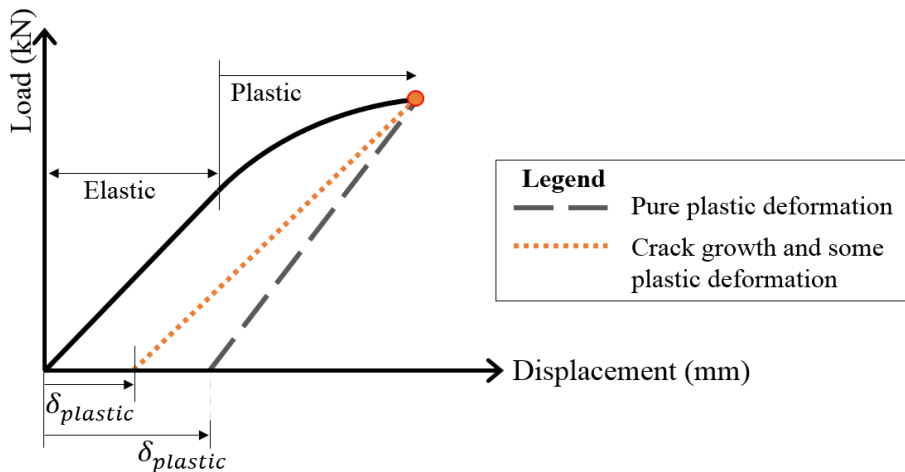


Figure 3.4: Load displacement graph showing two elastic unloads from a point in the plastic region. The dotted line shows the unload where both crack growth and plasticity has occurred, and the dashed line shows plasticity only.

The amount of plastic deformation may be found by either unloading completely to find the

x-intercept on a load displacement curve, or by inferring the x-intercept from a short unload of the sample, assuming the unload is linear-elastic. The latter technique is used in this project. With the use of regular partial unloads, stiffness and plasticity can now be decoupled.

3.3.2 Developing residual stress feedback loop in Matlab

The three bar rig residual stress equations were first implemented in a Matlab model. The simulation was designed to operate in the same way as the LabVIEW controller, dynamically responding to information about the specimen. Data feedback from the test machine was simulated with Electric Power Research Institute (EPRI) solutions. EPRI solutions are a well established set of analytical solutions that describe the elastic-plastic behaviour of a C(T) specimen, producing the data of a curve dependent on the specimen geometry and specified material properties. The solutions were originally developed by Kumar et al. (1984).

The aim of the Matlab simulation is to include the effect of an initial misfit, Δ_{misfit} , on the system and to see how the resulting residual stress developed. The simulation was carried out using the three different α conditions. One limitation of the EPRI solutions is that it is not possible to explicitly extract values of both specimen stiffness and plasticity at any point on the loading curve. However by assuming specimen stiffness remains constant, it is possible to use a partial unload, as described in section 3.3.1, to estimate the level of plasticity from the solutions. The effects of crack growth on the residual load are neglected. Despite this, the EPRI solutions allow development of the iterative control loop, and give insight into the effects of plasticity on residual stress.

A desired $P_{res}^{initial}$ was selected and the corresponding $\delta_{res}^{initial}$ was calculated. These values are chosen to be in the linear-elastic region. A $P_{res}^{initial}$ was selected as opposed to a Δ_{misfit} as this allowed the development of the residual load to be compared on the same scale across the three α conditions. This means that whilst $\delta_{res}^{initial}$ is constant, Δ_{misfit} is different for each α condition. By rearranging eqs. (3.9) and (3.11), for an initial linear-elastic residual load $P_{res}^{initial}$, Δ_{misfit} for all α conditions is given by:

$$\Delta_{misfit} = \left(\frac{\alpha + 1}{\alpha} \right) \delta_{res}^{initial} \quad (3.13a)$$

$$\delta_{res}^{initial} = \frac{P_{res}^{initial}}{k_{spec}^{initial}} \quad (3.13b)$$

substituting eq. (3.13a) into eqs. (3.10) and (3.11) gives:

$$\delta_{res} = \delta_{res}^{initial} - \left(\frac{\alpha}{\alpha + 1} \right) \delta_{pl} \quad (3.14a)$$

$$P_{res} = k_{spec} \left[\delta_{res}^{initial} - \left(\frac{\alpha}{\alpha + 1} \right) \delta_{pl} \right] \quad (3.14b)$$

$$= P_{res}^{initial} - \left(\frac{k_{spring}}{\alpha + 1} \right) \delta_{pl} \quad (3.14c)$$

where $\left(\frac{k_{\text{spring}}}{\alpha+1}\right)$ is the gradient of the relaxation of the residual stress.

At the start of the simulation, the specimen is loaded up iteratively to $\delta_{\text{res}}^{\text{initial}}$. Additional displacement is then applied in small increments. During the loading cycle small partial unloads are made every 0.1 mm. From these partial unloads, the gradient of the unload, k_{spec} , and its x-intercept, δ_{pl} , are calculated. These values are updated in eq. (3.14), and the remaining residual load and corresponding specimen displacement are found. The applied load is then completely removed, leaving only the residual load. The specimen displacement at this point, $\delta|_{P_{\text{applied}}=0}$, is given by:

$$\delta|_{P_{\text{applied}}=0} = \delta_{\text{res}} + \delta_{\text{pl}} \quad (3.15a)$$

$$= \delta_{\text{res}}^{\text{initial}} - \left(\frac{\alpha}{\alpha+1}\right) \delta_{\text{pl}} + \delta_{\text{pl}} \quad (3.15b)$$

$$= \delta_{\text{res}}^{\text{initial}} + \left(\frac{1}{\alpha+1}\right) \delta_{\text{pl}} \quad (3.15c)$$

where $\left(\frac{1}{\alpha+1}\right)$ is the gradient of the increase in specimen displacement, δ_{pl} , measured positive anticlockwise from the negative Y-axis. In fixed-load control this gradient tends to infinity, in fixed-displacement control, this gradient tends to 0. The specimen is then loaded back up and the simulation continues in this vein. A summary of this iterative process is shown in a data flow loop (fig. 3.5).

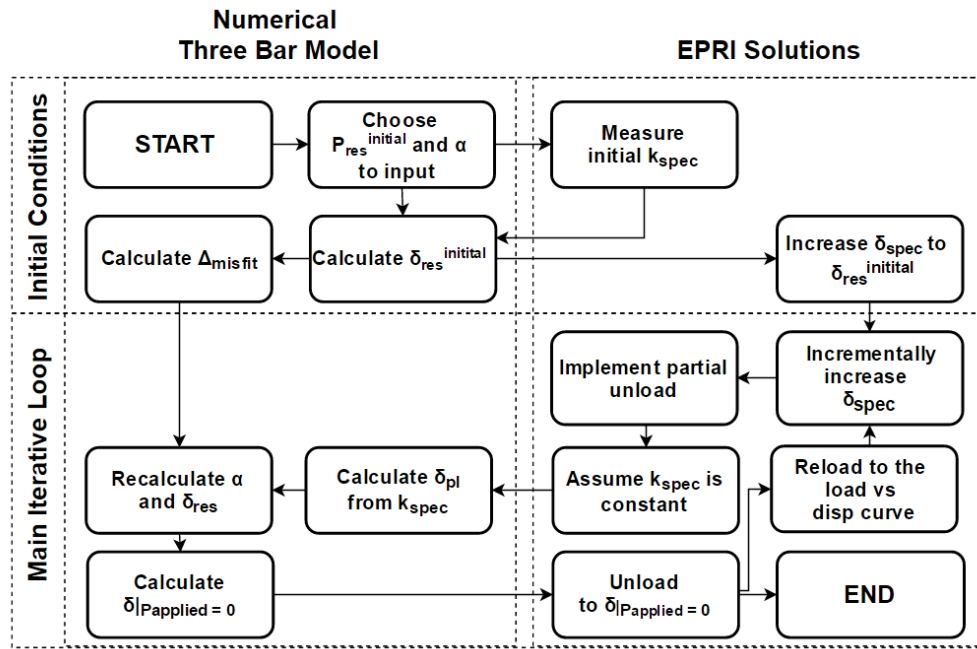


Figure 3.5: Initial conditions and iterative loop flow chart for the model including residual stress.

In the data flow loop it can be seen that the ‘theoretical specimen behaviour’ section, used in the elastic region, has been replaced by EPRI solutions to allow the simulation of elastic-plastic specimen behaviour. The loop shall be further developed in section 6 to incorporate experimental

complexities.

3.3.3 Matlab results

To validate the Matlab simulation and the control loop used, predictions of the expected behaviour must first be outlined and then compared to the simulated results. From eqs. (3.14b) and (3.15c), the results of the simulation can be approximated. In fixed-displacement control:

$$\alpha \rightarrow \infty \therefore \frac{\alpha}{\alpha+1} \rightarrow 1, \frac{1}{\alpha+1} \rightarrow 0 \quad (3.16)$$

substituting eq. (3.16) into eqs. (3.14c) and (3.15c) gives:

$$P_{res} = k_{spec} \left(\delta_{res}^{initial} - \delta_{pl} \right) \quad (3.17a)$$

$$\delta|_{P_{applied}=0} = \delta_{res}^{initial} \quad (3.17b)$$

as more plastic deformation occurs, P_{res} decreases, but $\delta|_{P_{applied}=0}$ does not change. Hence, the specimen unloads to the same displacement despite increasing plasticity. It is expected that residual load will reduce at the onset of plasticity. Physically, the maths represents the reduction in residual load as it is directly shed from the specimen to the outer region of the structure, due to the low compliance of the parallel springs, through plastic deformation. This agrees with literature representing the case where elastic follow up factor, $Z = 1$ and reduction in residual loading is greatest.

On the other hand, in fixed-load control, where α is very small;

$$\alpha \rightarrow 0 \therefore \frac{\alpha}{\alpha+1} \rightarrow 0 \quad (3.18)$$

substituting eq. (3.18) into eqs. (3.14c) and (3.15c) gives:

$$P_{res} = k_{spec} \delta_{res}^{initial} \quad (3.19a)$$

$$\delta|_{P_{applied}=0} = \delta_{res}^{initial} + \delta_{pl} \quad (3.19b)$$

as shown, P_{res} does not change with increasing plastic deformation, but $\delta|_{P_{applied}=0}$ increases. Therefore, it is expected that in fixed-load control the residual stress will not diminish despite increasing plasticity. Physically, this represents a structure where the cracked central region has a much higher stiffness than the outer region, hence, the specimen takes the vast majority of the load. Plastic deformation does not reduce the residual load in the specimen as the outer springs elongate with little load addition. This agrees with literature representing the case where elastic follow up factor, $Z = \infty$ and reduction in residual loading is zero.

The results of the Matlab simulation agreed with the expected behaviour stated above. Fig. 3.6 shows the main results of the simulation in which the unloaded specimen load and displacement are shown for three α conditions.

The specimen is initially loaded to $\delta_{res}^{initial}$, as shown by the dashed line. $\delta_{res}^{initial}$ is not a function of α thus is equal for all three load conditions. From this point applied displacements are added (solid line). Partial unloads (dotted lines) take place to measure k_{spec} and δ_{pl} . Using these values, the remaining residual load is calculated and unloaded to (dotted lines). Three dot-dashed lines join the end points from these unloads, at which $P_{applied} = 0$.

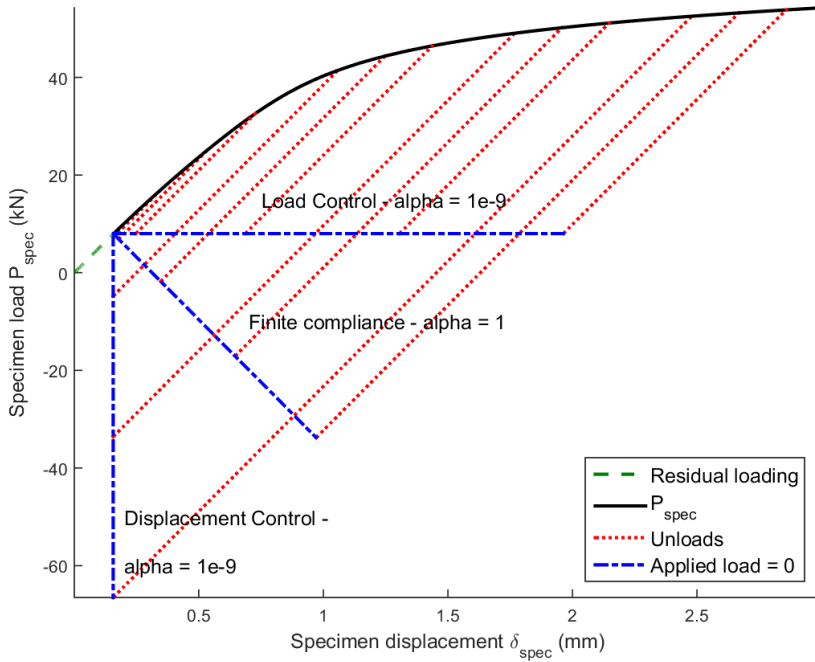


Figure 3.6: Development of residual stress for the three α conditions. Dashed (green) line represents $\delta_{res}^{initial}$. Dot-dashed (blue) line represents the remaining residual stress after unloads for the different α values.

Fig. 3.7, uses the calculated values of P_{res} to decouple the components of $P_{applied}$ and P_{res} that sum to give the overall load, on the specimen. The components of load are plotted against δ_{spec} as to show the components development as displacement is increased.

Under fixed-load control the residual load can be seen to remain constant, on figs. 3.6 and 3.7 as δ_{spec} or more importantly as δ_{pl} increases. Shown in eq. (3.19a) this takes place because δ_{pl} does not act to reduce load, due to the very low α . P_{res} remaining constant acts to decrease the $P_{applied}$ required to produce the same P_{spec} , this is shown in fig. 3.7.

In fixed-displacement control the residual load is seen to decrease vertically, with no increase in $\delta|_{P_{applied}=0}$. This is because any plasticity directly reduces the level of residual stress in the system, as shown by eqs. (3.17a) and (3.17b). The P_{res} can be seen to go negative, this is because the amount of plasticity taking place is larger than the initial size of the misfit, causing the residual force to act in the opposite direction to the applied loading. Figure 3.7 (c), displays the effect of the decreasing residual load on the applied load. It can be seen from the figure that $\delta_{applied}$ must increase to a higher value than δ_{spec} due to the negative δ_{res} .

For the finite compliance load condition of $\alpha = 1$ residual load evolves in a manner between the two boundary conditions. δ_{res} reduces, unlike in fixed-load control, but at a slower rate than

the fixed-displacement controlled loading due to more compliance in the system. Increasing α , thus decreasing the level of elastic follow-up would therefore act to reduce the rate of relaxation of δ_{res} , aligning with the literature reviewed in section 2.

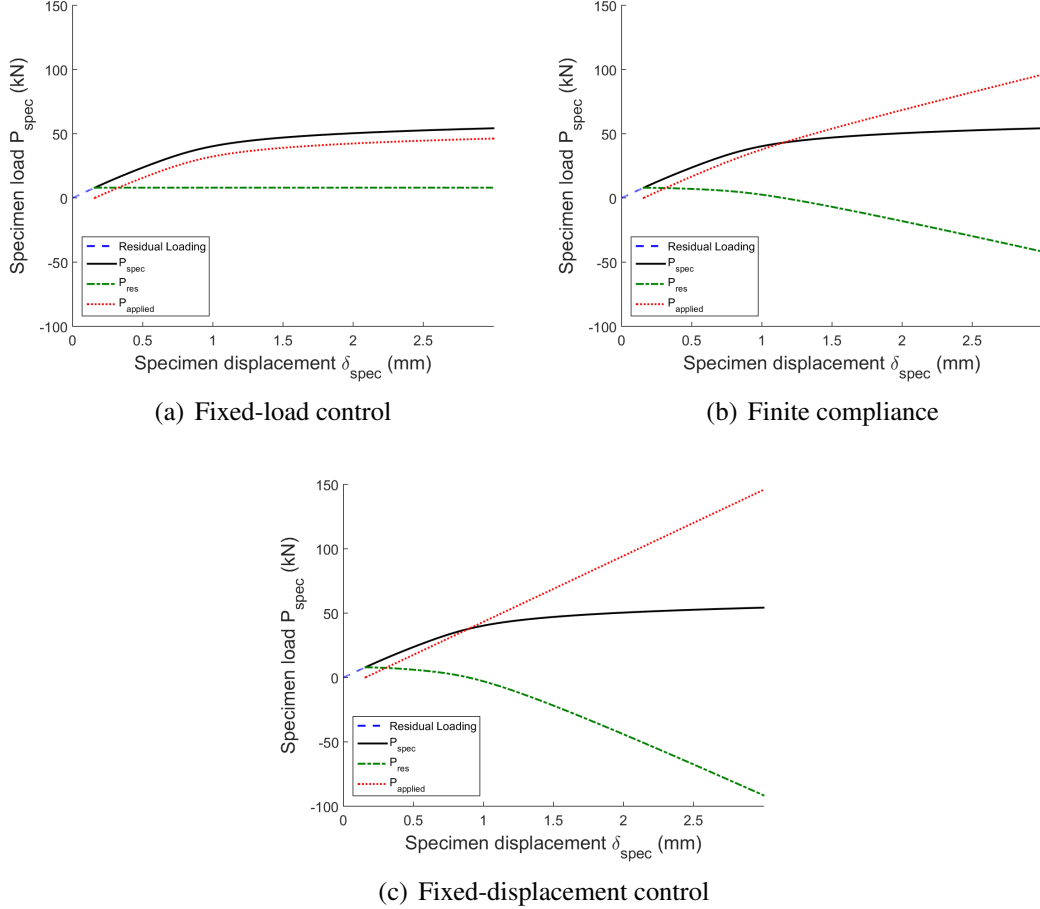


Figure 3.7: Effect of load applied to the specimen on residual stress in the specimen for (a) fixed-load control (b) finite compliance (c) fixed-displacement control loading conditions.

These results validate the analytical model which has been built and simulated in Matlab and can now be incorporated into the LabVIEW program. It is good to note that the graphs produced by the iterative Matlab script in fig. 3.7 are concurrent with those seen in fig. 2.6 from Aird (2009). This shows that the Matlab model and data flow used is correct.

It is important to note that the EPRI solutions do not allow accurate decoupling of crack growth from plasticity. However, the method to implement partial unloads developed through the simulation remains valid. Experimental test data is required for partial unloads to obtain accurate measurements of k_{spec} and δ_{pl} as explained in 3.3.1. To extend the Matlab simulations outlined in this section to LabVIEW and real testing, the experimental set-up and measurement techniques need to be outlined.

4 Materials and methodology

In this section, the methods by which the algorithms are implemented in the laboratory are examined. Firstly, the aluminium C(T) specimen used in the experiments is presented followed by an explanation of the Instron tensile test machine that was selected. Next, the processes used to measure crack length and specimen displacements are explained in detail. The latter is done using a video extensometer and clip gauge. Finally, the manner in which the LabVIEW is interfaced with the Instron machine controller is described.

4.1 Aluminium Compact Tension Specimen

Throughout experimental testing ASTM Active Standard E399 Compact Tension (C(T)) test specimens were used, with dimensions specified in the Appendix (fig. A.1). These specimens are commonly used in fracture toughness assessments, where the W/T ratio is 2 in order to maintain a plain strain condition at the centre of the specimen (ASTM International, 2013). Under plain strain conditions, materials should behave elastically until the fracture stress is reached. These specimens are usually made with a fatigue pre-crack, as this creates a sharp crack tip, which has a higher stress concentration factor. The high stress concentration factor at the crack tip expedites brittle fracture. When investigating the effects of plasticity on the evolution of residual stress, sufficient amounts of plastic deformation would be required. To facilitate plastic behaviour the three specimens were not pre-cracked to allow ductile fracture to occur.

The material Aluminium AL 6082 T6 was chosen due to its availability and ease of manufacture. It also has a reasonably low stiffness and high ductility, with a Young's modulus and yield strength of 70 GPa and 240 MPa respectively (Alfano et al., 2008). This made specimen elastic and plastic deformation more observable over a smaller loading range, in comparison to other materials such as steel. An illustration of the C(T) specimen geometry is shown in figure 4.1.

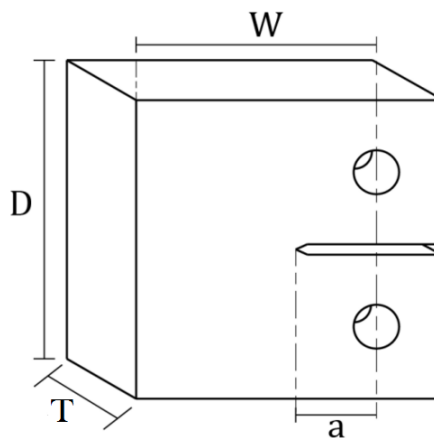


Figure 4.1: ASTM Active Standard E399 C(T) specimen geometry

4.2 Instron Servo-hydraulic test machine

Through experimental measurement, it was found that the load at which the C(T) specimen reaches its yield strength is between 30 to 35 kN. Therefore, a machine with load capacity larger than 35 kN was chosen. In order for the test machine to simulate the load applied on the specimen by the three bar rig, it has to be able to receive signals from an external source running an algorithm. This requires the controller installed on the machine to have an auxiliary input channel. Based on these requirements, a 100 kN capacity Instron servo-hydraulic test machine installed with an Instron 8800 controller was chosen over the other machines with the same capacity, such as the Zwick electro-mechanical machines.

Clevis grips and loading pins were used to fix the specimen in place, as seen in fig. 4.2. The load through the specimen and grips was measured by the machine's internal load cell. The displacement of the machine's piston, which is the total displacement of the grips and the specimen, was measured by the machine's built-in Linear Variable Differential Transformer (LVDT). These measurements are tracked by the Instron 8800 Controller, and are displayed on the computer through a basic programme named Instron console.

The Instron's Wavemaker, which is a basic block control programme, is generally used together with Instron console and the machine to apply a load in either load or displacement control. Wavemaker is installed on the same computer. Similarly, it uses measurements from the load cell and the LVDT in control and data logging. Wavemaker is capable of only basic ramp, hold, and cyclic loading regions (Instron Wavemaker, 2016). Initial tests were done with Wavemaker in both load and displacement control before more complex testing was undertaken using Labview programming.

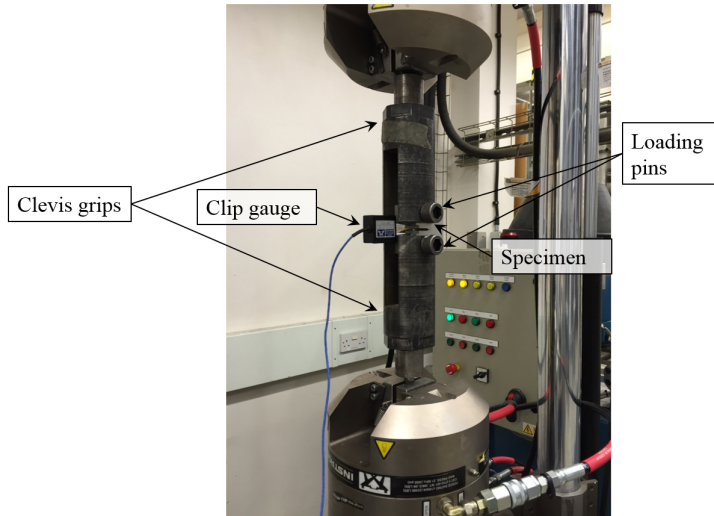


Figure 4.2: Photograph of the clevis grips and loading pins used with the Instron servo-hydraulic machine

4.3 Measuring δ_{CMOD}

The crack mouth opening displacement, δ_{CMOD} , is defined as the distance between the two knife edges at the opening of the crack, as shown in fig. 3(a). It was measured using a clip gauge, as shown in fig. 3(b). The clip gauge has a gauge length of 10 mm and is calibrated for a travel length of 4 mm from the gauge length (Instron CMOD, 2016). The knife edges on the specimens held the clip gauge in place, as shown in fig. 3(b). δ_{CMOD} measurements from the gauge were recorded in Wavemaker.

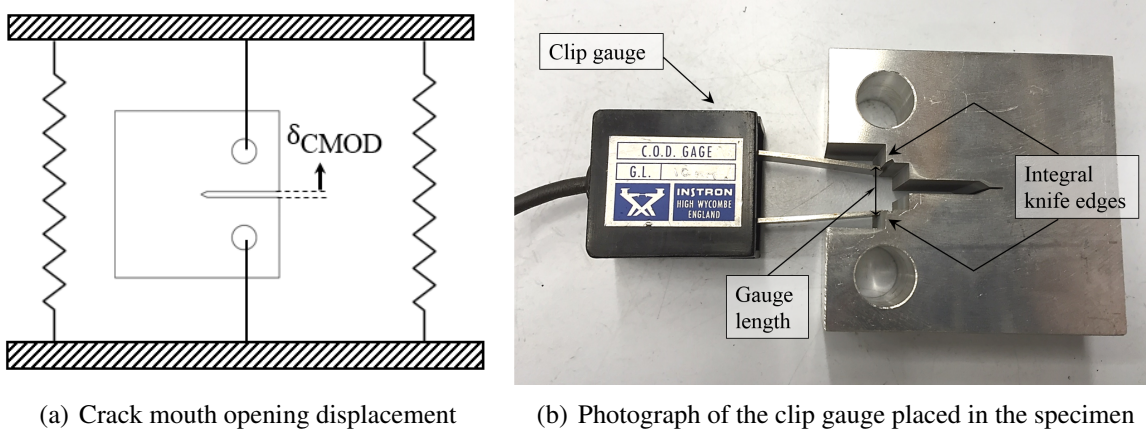


Figure 4.3: Measuring Crack mouth opening displacement

4.4 Measuring δ_{spec}

In order to have a valid reading for specimen displacement, a means of measurement must be found. To this end, a video extensometer was set-up to track the movement of the specimen at a number of points. This tracked selected features from live video and measured displacements of external surface features. Due to the experimental set-up, it was not possible to get a front on view of the pin holes (point D, as shown in fig. 4.5) due to the pin heads obstructing the view, and the pin heads moving relative to the specimen. The video extensometer was set-up with a side-on view (fig. 4.4). This still did not allow a direct reading of the pin hole displacement. Instead, three displacements (A, B and C) were tracked (shown in fig. 4.5) during a simple monolithically increasing load test.

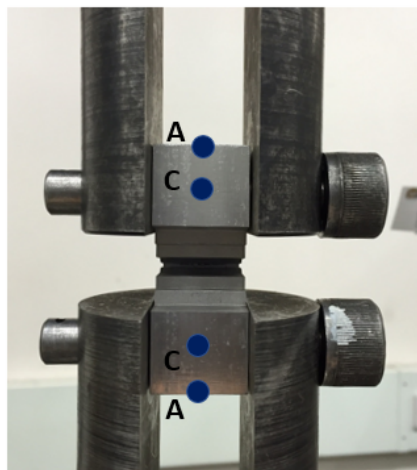


Figure 4.4: Side view of the CT specimen, showing the general area measured by the Video extensiometer. The extensiometer is located behind the viewer.

In order to calibrate the video extensiometer readings for data processing, δ_{CMOD} was tracked by the video extensiometer and compared to the data from a clip gauge which was set-up on this same test. This allowed a translation of the video extensiometer data from pixels to mm by matching the two data sets. Matching this data also synced time stamps between the two sources.

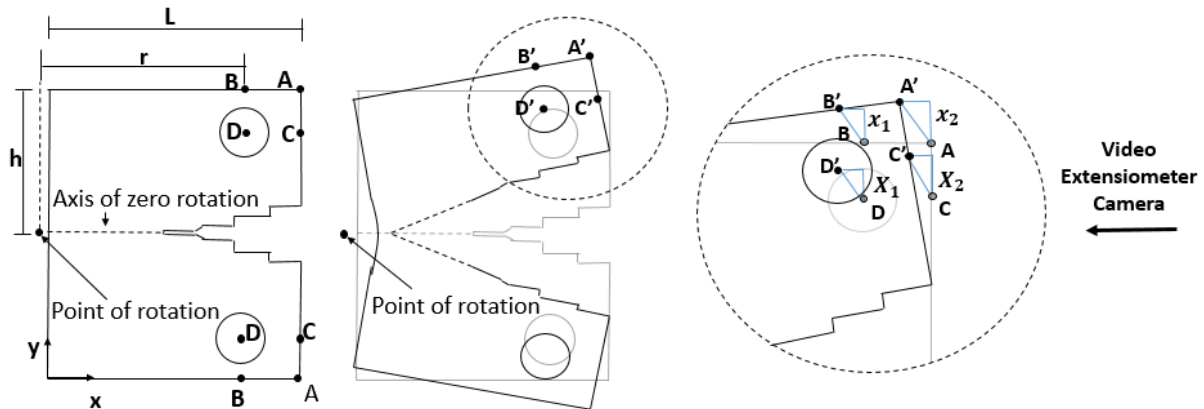


Figure 4.5: Front view of the CT specimen, showing the locations measured by the video extensiometer A, B, C. These are used to infer the displacement at D, the specimen displacement. The video extensiometer is located some distance to the right of this diagram, facing horizontally side on.

Assuming points A, B, C and D maintain their relative distances from each other, from trigonometry, it can be shown that there is a relationship between the displacement A and B that accounts for this rotational difference as seen in eq. (4.1).

$$B = \frac{r^2 A}{r\sqrt{L^2 - A^2} + hA} \quad (4.1)$$

Here r is the initial horizontal distance from the centre of rotation to B, L is the length of the

specimen and h is the initial vertical height of A and B from the horizontal axis of symmetry.

The only unknown here is r . By using measured data for A and B, the value of r can be deduced by finding the value that produces the least squares difference between the two sets of displacement data for points A and B. This formula can then be applied to extrapolate D (which is not measured) from the data collected for C. Using eq. (4.1), and substituting C for A and D for B, and adjusting the value of h accordingly, gives a value of specimen displacement D (equal to δ_{spec}) throughout the experiment.

4.5 Measuring crack length

The nature of elastic-plastic testing means that both plastic deformation and crack growth take place. When significant plasticity took place, shear lips and ‘dimple’ like structures formed on the outer faces of the specimen. As a result, the crack length visible on the outside face was not representative of the crack length on the inner face of the specimen. Fig. 4.6 shows the outer face (right) and inner face (left) of one of the CT specimens. It is evident that the crack on the outside surface does not reflect the internal crack for the majority of the structure. Specimens were then cut in half as shown in fig. 4.6 and the crack lengths on the internal face of the specimens were measured.

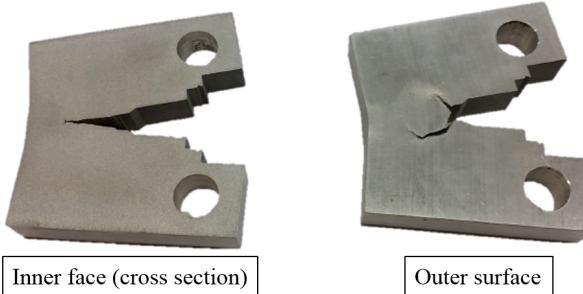


Figure 4.6: Crack length on the outer and inner face of a plastically torn specimen, cut in half along the central XY- plane.

4.6 LabVIEW programming tools

LabVIEW (National Instruments Corporation, 2015) a graphical programming language set in a system design environment. It is generally used for instrument control, data acquisition and automation. Programmes and functions are written as Virtual Instruments (VI) in LabVIEW. It was chosen as the platform for the control algorithm because the hardware required to interface it with the machine was readily available.

A few of the key programming tools used in LabVIEW will be highlighted and images are shown in the appendix. Signals were sent to and received from the machine through data acquisition (DAQ) VIs (fig. A.2(a)). These signals were logged as data in a ‘write to measurement’ VI (fig. A.2(a)). Stiffness readings were made using a ‘Linear fit’ VI (fig. A.2(b)), which fits the data to a linear regression and measures the slope and intercepts. Case structures

(fig. A.2(c)) were used to run functions in a specific sequence. Conditional terminals (fig. A.2(d)) were used in while loops to set the limits to the iterations. Shift registers were used to hold and transfer data between case structures. Fatigue cycles were set up using a ‘Sinewave generator’ VI (fig. A.2(e)).

4.7 Interfacing with the Instron Test Machine

LabVIEW runs on a computer, which is connected via USB to a data acquisition (DAQ) hardware module. LabVIEW bypasses Instron Wavemaker and communicates directly with Instron’s Console and 8800 controller via analogue cables. The DAQ model used is USB-6211 from National Instruments. The set-up is illustrated in fig. 4.7.

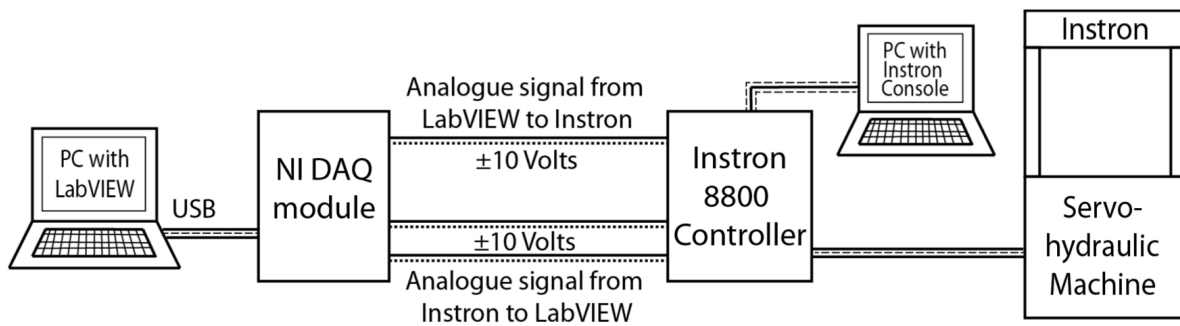


Figure 4.7: A schematic of the experimental set-up.

Measurements of load and displacement were received by LabVIEW as voltage signals from the Instron controller. Similarly, the Instron controller received displacement demands from LabVIEW as voltage signals. These signals were sent and received through the DAQ hardware module and DAQ VIs. The magnitude of signals are limited by the ± 10 V capacity of the DAQ hardware module.

The DAQ VIs used in the LabVIEW VI were configured with the same voltage to mm and voltage to kN conversion factors as those set in Instron console. These factors were adjusted according to the expected range of load and displacement for each test.

5 Testing measurement accuracy

In order to implement the algorithms developed in section 3, the equipment and testing procedures must be scrutinised, all added dynamics accounted for in the algorithms and any limitations recognised when testing and analysing results. This section of the report aims to validate the methods used and measurements taken.

5.1 Decoupling crack growth and plasticity

Section 3.3.1 describes the method of partial unloading to find specimen plasticity and stiffness. This strategy was initially implemented in Instron Wavemaker and the data was analysed in Matlab to validate the results. It is important to note that the displacement measured in this subsection is total displacement δ_{total} , which does not account for machine dynamics (explained in section 5.3). Therefore the stiffness measured from an unload is k_{total} , but plasticity δ_{pl} is unchanged.

Using Instron Wavemaker, a specimen was loaded up and then partially unloaded, at regular intervals, after plastic deformation had occurred. The specimen was loaded in fixed-displacement control as opposed to load control so as to obtain the full range of displacement data. The unloads were activated manually using a block transfer button in Wavemaker. This was repeated 20 times periodically at approximately 0.5 mm intervals of total displacement. A significant amount of plastic tearing was seen on the specimen, which indicated that the effects of both plasticity and crack growth should be observed in the data. The results of the test are shown in figs. 5.1 and 5.2. The elastic-plastic curve is shown in fig. 5.1. The gradients and x-intercepts of the unloads were measured and plotted against the unload index as shown in fig. 5.2.

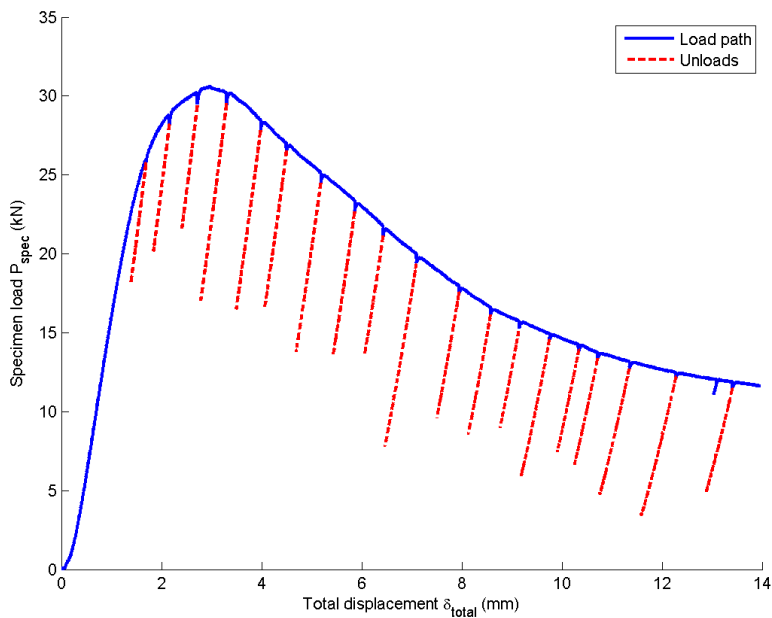


Figure 5.1: Load-displacement plot demonstrating partial unloads.

As seen in fig. 5.2, with exception to the first three data points where significant crack growth has not yet taken place, the stiffness decreases and plasticity increases with each unload as the specimen plastically tears. This aligns with behaviour expected from plastic tearing. In this instance, the stiffness and plasticity trends appear to be linear over the measured region. However, these linear trends seen may not always be the case, as the specimen behaviour is dependent on the loading condition and material properties such as grain direction which may cause brittle fracture to occur. Brittle fracture would lead to sharp drops in stiffness for the same plasticity.

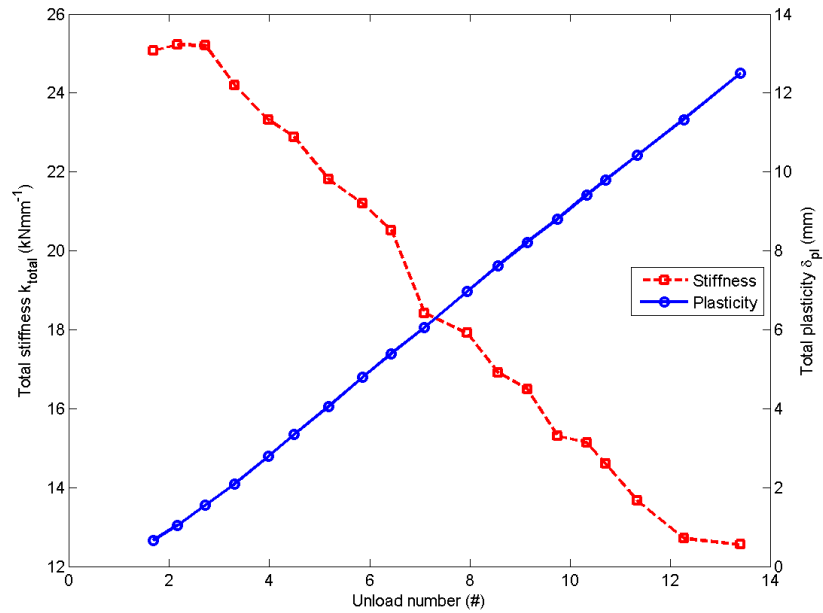


Figure 5.2: Stiffness k_{total} and plasticity δ_{pl} found from periodic unloads under a continually increasing δ_{total}

By reading δ_{pl} and k_{total} from the partial unloads and taking the value of δ_{total} at the top of the unload, it is possible to calculate P_{spec} . To validate the reliability of the readings from each unload, a comparison of real load data to calculated P_{spec} , at the top of each unload, can be made. P_{spec} can be calculated from Hooke's law where the magnitude of elastic deformation can be calculated by subtracting δ_{pl} from δ_{total} :

$$P_{spec} = k_{total}(\delta_{total} - \delta_{pl}) \quad (5.1)$$

If the readings of δ_{pl} and k_{total} are reliable, the calculated P_{spec} should map onto the point on the real load line at which the unload is undertaken.

The most recent values of δ_{pl} and k_{total} , taken from the latest unload, can be used to calculate P_{spec} in an iterative manner. These values of δ_{pl} and k_{total} will then remain constant while δ_{total} increases until they are updated on the next partial unload. Using Matlab to create a simulation of this iterative loop, a line shown on fig. 5.3 was produced.

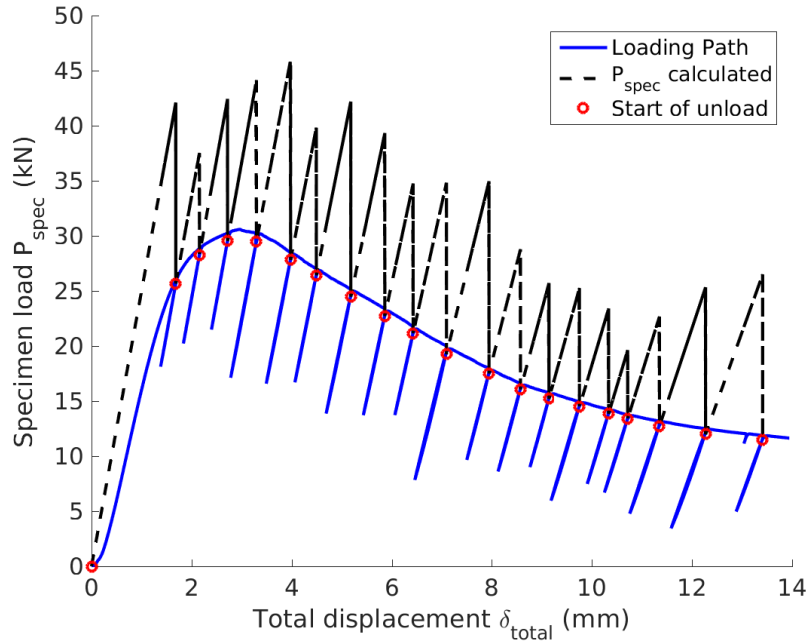


Figure 5.3: P_{spec} calculated from stiffness and plasticity reading plotted against total displacement. Each time a partial unload is made, and δ_{pl} and k_{total} are updated, this results in the calculated P_{spec} reattaching to the actual loading path.

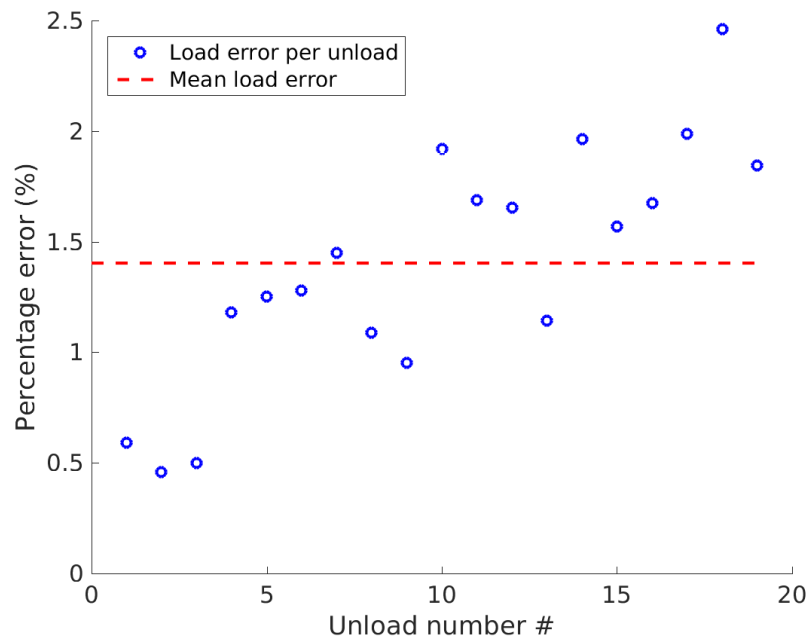


Figure 5.4: This graph shows the percentage error between the actual load at the start of an unload, and the load calculated using eq. (5.1). The dotted line is the mean of percentage error.

Fig. 5.3 shows that the calculated load path follows the real loading path, converging at the top of each unload and diverging in between. It is only at the top of the unload that P_{spec} calculated will be accurate as this is the point at which the unload readings are valid.

It is important to note that values of plasticity and stiffness are only known during the linear-elastic unload. Once additional displacement has been applied, further plasticity and crack growth occurs, hence they become unknown values. The best estimations for these values are given by the most recent partial unload, so the more regular the unloads the better the resolution. Increasing the frequency of the unloads will increase the resolution, which allows the calculated load path to better track the real load line.

Fig. 5.4 displays the percentage error between the calculated and actual P_{spec} at the start of each unload. This percentage error is a measure of the accuracy the calculated P_{spec} readings. From this the reliability of the stiffness and plasticity measurements can be inferred. The results show a very small error on each of the unload over a range of δ_{total} from 0 mm to 14 mm, which is more than sufficient for later testing. The mean error of 1.4% and a maximum of 2.46%.

The measurements of k_{total} and δ_{pl} have firstly been shown to follow expected trends in fig. 5.2 and then to produce accurate P_{spec} values by comparing real load data to calculated. Thus partial unloads have been shown to take accurate readings of the x-intercept and gradient of the unload. What these variables represent physically will depend on the displacement input. Partial unloads can now be implemented further with confidence in the precision of the readings.

5.2 Validation of stiffness measurements

In section 3.3.1, the concept of a partial unload as a method to quantify stiffness and hence plastic deformation was explored. The accuracy of these stiffness measurements were verified in section 5.1. In order to gain more confidence in the readings, experimental stiffness measurements obtained were validated through comparison with theoretical solutions for specimen stiffness. In this subsection, the effects of crack growth (fatigued and plastic tearing) and plasticity on stiffness are investigated, then the reliability of the unload gradients as a measure for specimen stiffness is assessed. It is found that the compliance of the machine has an influence on the application of displacements on the specimen and the readings recorded by the Instron controller.

5.2.1 Comparing stiffness and crack length in different failure modes

In theory, using eqs. (3.5) and (3.6), the crack length, a , of any two specimens with the same elastic stiffness should be the same. The measured stiffness should be unaffected by plasticity. If it can be shown that the crack length in two specimens is the same, whether the crack is formed by from fatiguing or plastic tearing, then this can be used as a check that plasticity is not affecting stiffness and confirm that the equations and methods used are valid. Thus an unload can perfectly decouple the two failure modes.

To confirm that the elastic stiffness of a specimen is dependent on crack length alone and not affected by the mode of crack propagation (fatigue crack growth or plastic tearing), two specimens were tested. One specimen was loaded in tension to cause plastic tearing and its stiffness was recorded. The second specimen was then fatigued to the same stiffness as the

plastically torn specimen, using a LabVIEW algorithm that measured stiffness from the gradient of the fatigue cycling.

Table 1: A table showing the measured crack lengths for of equal elastic stiffness.

Specimen	Elastic Stiffness (kNm^{-1})	Predicted crack length from stiffness (mm)	Actual crack length (mm)
Plastically torn	12.481	35.7	38.0
Fatigued in LabVIEW	12.287	35.9	35.0

The results in table 1 show that there is not identical crack length for identical stiffness of the two specimen. The plastically torn specimen has a longer crack at the centre of the specimen than the specimen which was fatigued to produce crack growth. The crack in the plastically torn specimen was 8.6% longer compared with the fatigued crack length. This would seem to suggest that crack length is dependent on the means by which the crack propagates.

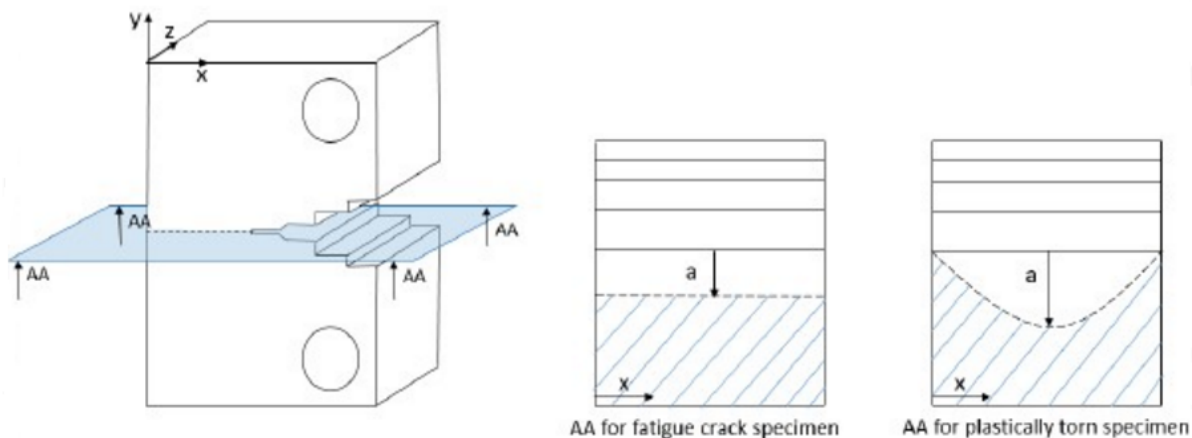


Figure 5.5: A schematic of the section view of the two areas compared to confirm the readings of similar stiffness.

However, crack length may not constant across the width of a specimen, dependant on loading region. As demonstrated in fig. 5.5, the crack length in the specimen is a function of position x . Thus the remaining area of contact (and hence elastic stiffness) is dependent on the function relating crack length, a , and position, x .

The elastic fatigue tear was approximated as a crack of constant crack width. For the plastic tear the function relating these parameters was assumed to be approximately a quadratic parabola. The quadratic was found to be $F(x) = 0.051x^2$.

The contact areas are compared in Table 2. Area was found to be a much better metric when comparing equal elastic stiffness. The remaining difference is supposed to be due to the fact that the profile of the contact area is unlikely to be given by an exact parabola. This results in the relationship between crack length and elastic stiffness being much more complex once plastic tearing has occurred. It is likely to be even more difficult if a combination of plastic tearing and fatigue loading has occurred.

Table 2: A table showing the contact area for specimens of equal elastic stiffness.

Specimen	Elastic Stiffness ($kNmm^{-1}$)	Predicted contact area from stiffness (mm^2)	Actual contact area (mm^2)
Plastically Torn	12.481	356	367
Fatigued in Labview	12.287	353	375

In summary, these tests confirmed that we can be confident in using periodic unloads to decoupled readings for stiffness and plasticity. The stiffness measurements calculated from unloads have been shown to be unaffected by the presence of plasticity. Minimum cross-sectional area, which is known to correlate with actual specimen stiffness, is identical for specimens with the same stiffness as measured from an unload, regardless of crack growth mechanism. However there is still a requirement to check that the values obtained for stiffness match that expected from theory.

5.2.2 Comparing stiffness measurements with theory

It is important to confirm that the unload gradient gives the correct stiffness values as found from theory. To this end, a specimen was taken, fatigued, and the gradients of the last 10 unloads averaged. The specimen was then plastically torn until complete failure. This meant that the crack growth due to fatigue cycling was visibly different to the plastic tearing area on the specimen surface (in plane-AA as defined in fig. 5.5). This allowed the crack length for the last fatigue cycle to be found. For these values of a/W , the theoretical stiffness of the specimens was calculated. The results are shown in Table 3.

Table 3: A table comparing measurements and theoretical calculations of stiffness for different crack lengths.

Crack length, a (mm)	Measured Stiffness ($kNmm^{-1}$)	Theoretical Stiffness ($kNmm^{-1}$)
25	24.37	47.31
31	16.76	24.53
39	6.36	7.08

When comparing the specimen stiffness found experimentally from the gradients of the unload and the analytical solution (eqs. (3.5) and (3.6)) for the stiffness for the given a/W , it was found that there was a significant discrepancy between the two values. If the measured stiffness is much less than the expected stiffness from theoretical calculations, there must be added compliance in the system. This is assumed to be compliance inherent to the machine and the validity of this assumption and its implications are discussed in section 5.3.

5.3 Machine compliance

As demonstrated in section 5.2.2 stiffness readings measured by the Instron controller, do not match the theoretical specimen stiffness calculations, eqs. (3.5) and (3.6). This discrepancy is likely to be caused by machine compliance in the experimental set-up. Machine compliances is a critical source of error in the measurements as it reduces the real displacement applied to the specimen. The displacement input by the Instron controller is not equal to the displacement of the specimen ($\delta_{total} \neq \delta_{spec}$). It is important to note that the compliance of the machine can be modelled by a spring in series with the specimen, thus the load in the specimen and the machine are equal, and shall be referred to as P_{spec} . Fig. 5.6 shows a schematic drawing of machine compliance in the system.

To ensure the specimen receives the correct displacement, hence, that stiffness measurements are correct, the effect of machine compliance must be quantified. Once quantified and validated, machine compliance may be incorporated into the controller algorithm. In order to correctly apply a desired δ_{spec} , or to correctly read k_{spec} during an unload, the machine displacement, $\delta_{machine}$, and machine stiffness, $k_{machine}$, must be accounted for.

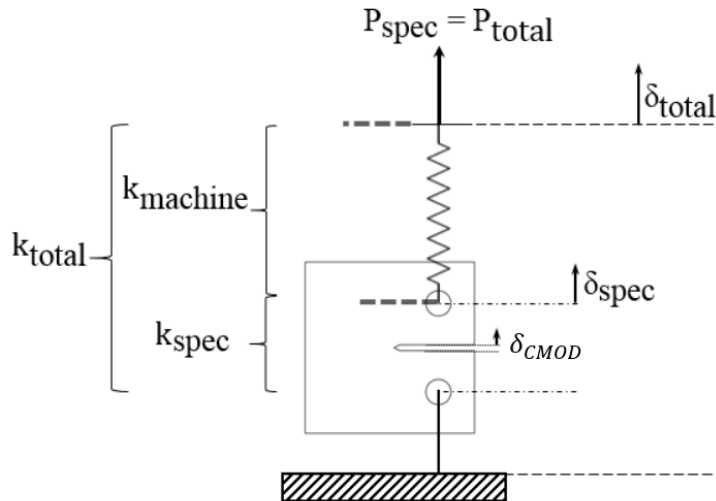


Figure 5.6: Schematic drawing of machine compliance, showing relationships between total, specimen and machine compliances and displacements.

It is assumed that the machine and clevis grips behave elastically under loads experienced during testing. This compliance can be modelled as a spring in series with the specimen. Fig. 5.6 shows the machine-specimen set-up. $k_{machine}$ is therefore given by:

$$\frac{1}{k_{total}} = \frac{1}{k_{machine}} + \frac{1}{k_{spec}} \quad (5.2a)$$

$$k_{machine} = \frac{k_{total}k_{spec}}{k_{spec} - k_{total}} \quad (5.2b)$$

where k_{total} and δ_{total} are measured by the Instron controller.

Fig. 5.7 highlights the essential difference between the work presented in this report and

the work done previously by Aird (2009). In Aird's testing, the entire three bar rig was present in the experimental set-up and so the machine compliance is incorporated in series with the three bar rig. In the work presented in this report, only the physical specimen is present in the experimental set-up and consequently the machine compliance is incorporated in series with the specimen *within* the three bar rig.

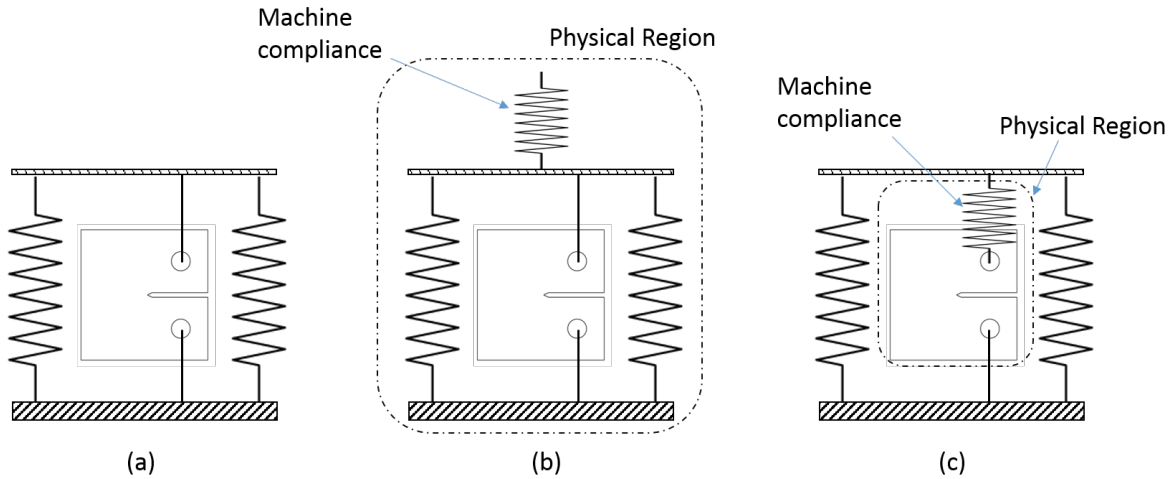


Figure 5.7: Three interpretations of the three bar model. (a) theoretical (b) physical (as modelled by Aird (2009)) (c) simulated with feedback control loop (as produced in this project)

Firstly, the extent to which the machine compliance is effecting the experiments must be assessed. If the machine was sufficiently stiff, the effects of machine compliance would be negligible. To show that this is not the case a measure of displacement that does not include machine effects can be compared to the input displacement. Crack mouth opening displacement is easily measurable, using a clip gauge, and does not include machine effects. Hence, a clip gauge was fitted onto the specimen at the crack mouth and a tensile test to failure with regular unloads was performed. The displacements of the clip gauge, δ_{CMOD} , and the Instron controller, δ_{total} , were recorded. The results are shown in fig. 5.8.

The results show that the values for displacement measured by the clip gauge are vastly different to those measured by the Instron controller. A possible explanation of the discrepancy is that the elastic strain in the region between the crack mouth and the pin holes causes extension. However, the difference is too large thus the reason for the discrepancy must be due to added compliance in the system. This compliance is due to finite stiffness of the machine, $k_{machine}$.

One method that could be used to quantify the machine compliance is to run a tensile test with an extremely stiff material pinned into the clevis grips. This would make k_{spec} infinity stiff and isolate $k_{machine}$, so that it can easily be evaluated. Unfortunately, due to practical restrictions, such as the geometry of the clevis grips, a piece of material with a sufficiently large stiffness could not be used.

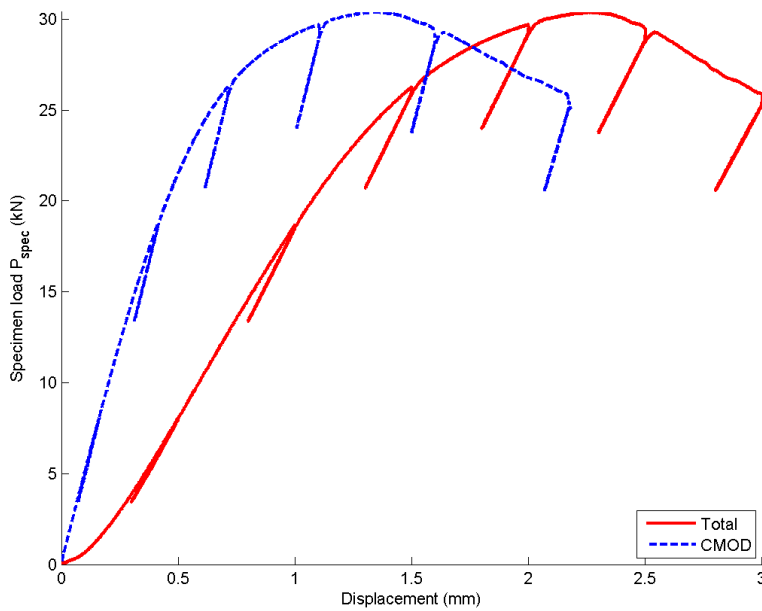


Figure 5.8: A plot showing the difference between total displacement measured by the Instron controller to crack mouth displacement.

It is important to note that directly measuring specimen displacement during testing is difficult due to the experiential set-up. The video extensiometer (used as described in section 4.4) is not easy to interface with the LabVIEW code used to run experiments and requires readings of δ_{CMOD} from a clip gauge to calibrate the readings from pixels to mm (see also section 4.4). Using a clip gauge to allow the implementation of a video extensiometer is impractical as it will be damaged during fatigue testing and will limit the measurement range. A limited displacement range of testing is a disadvantage of the physical three bar rig and is something which is to be avoided during this project. Quantifying $k_{machine}$, using it to map onto k_{spec} then finding δ_{spec} from the values, removes the problems of direct measurement and provides an elegant solution.

5.3.1 Finding machine displacement

Firstly, to find machine compliance, machine displacement is required. By plotting machine displacement against load, the stiffness of the machine can be calculated. Using a direct measurement of δ_{spec} and the Instron input δ_{total} , machine displacement can be found.

$$\delta_{machine} = \delta_{total} - \delta_{spec} \quad (5.3)$$

The means by with δ_{spec} is measured is described in section 4.4. The three displacements δ_{spec} , δ_{total} and the difference between the two, $\delta_{machine}$, are plotted against P_{spec} on fig. 5.9.

From the solid line in fig. 5.9, the relationship between P_{spec} and $\delta_{machine}$ is seen to be linear up to around 27 kN, which is the yield point of the specimen. However, at this point the machine appears to exhibit non-linear behaviour. This is unusual, as the machine should not behave

plastically at such low loads, given its much larger yield strength relative to the specimen. One hypotheses made was plastic deformation around the pin holes. However, no visible plastic deformation was observed on the specimen after the test. Therefore, this trend is likely to be caused by errors in the video extensiometer readings in the plastic region, which arise due to a deviation from the trigonometric relationships assumed between points A, B,C and D.

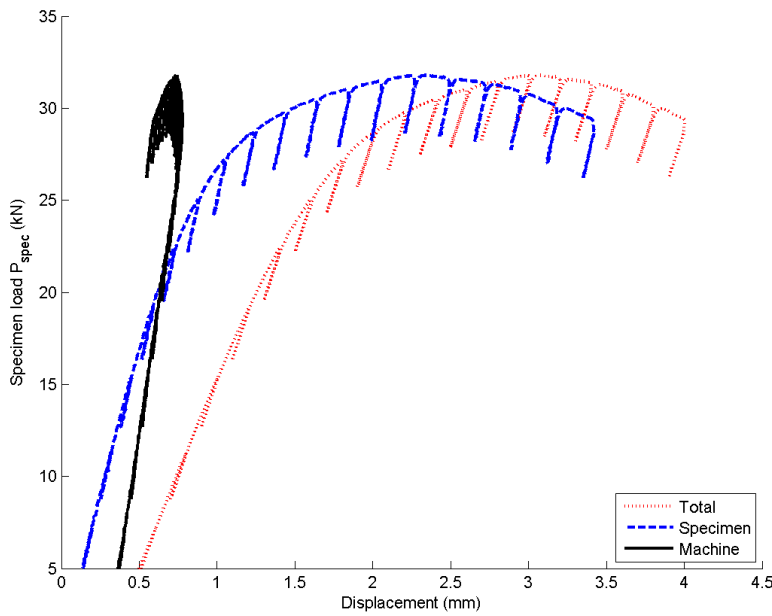


Figure 5.9: Plot of load P_{spec} against displacements. The graph shows total displacement, measured by the Instron, specimen displacement as measured by the extensiometer, and machine displacement; the difference between the other two displacements.

In relation to the feedback controller, the accuracy of the stiffness measurements are only important on the initial linear elastic load up, and on the elastic unloads. Therefore, the compliance of the machine was characterised only for these regions, and the reason for the unusual behaviour in the plastic regions were not thoroughly investigated.

5.3.2 Finding $k_{machine}$

Fig. 5.10 is a magnified plot of $\delta_{machine}$ against P_{spec} , thus, the gradient of the line represents machine stiffness, $k_{machine}$. Interestingly, two different gradients can be observed – one is the linear elastic gradient solid continuous line from 0 kN to 27 kN; the other is the gradients of the protrusions from this line is $k_{machine}^a$. To account for these different gradients two variables are introduced: $k_{machine}^a$ as the gradient of the partial unloads, and $k_{machine}^b$ as the gradient of the initial load up.

$k_{machine}^b$ can easily be found from a line of best fit on the data from 0 kN to 27 kN, as indicated by the solid red line on fig. 5.10. It was found that $k_{machine}^b = 56.1 \text{ kNm}^{-1}$.

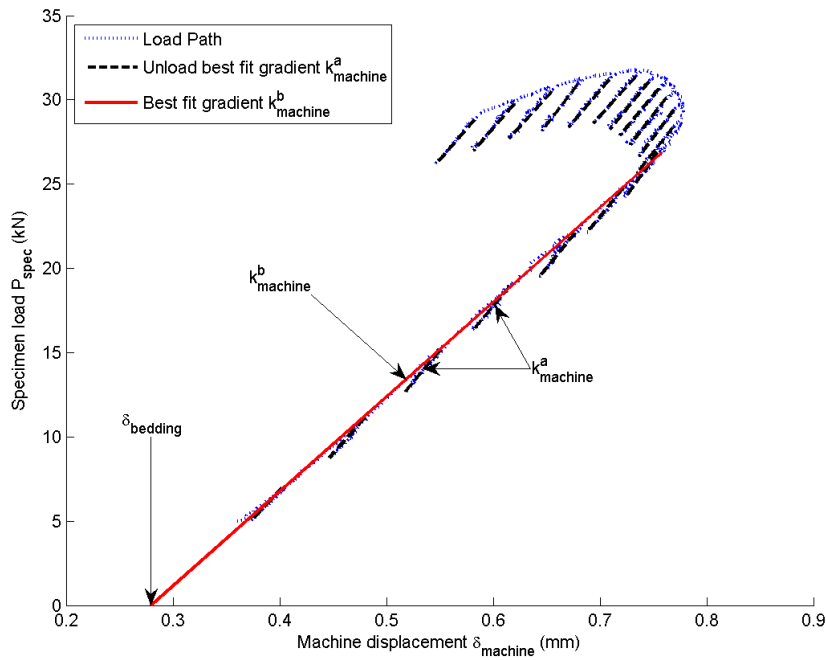


Figure 5.10: Plot of P_{spec} against $\delta_{machine}$ in dotted (blue), showing the elastic region (up to 27 kN) line of best fit in solid (red), and the anomalous non-elastic region above that. Note: the paths described by the unloads are clearly visible as the periodic features descending from the main line.

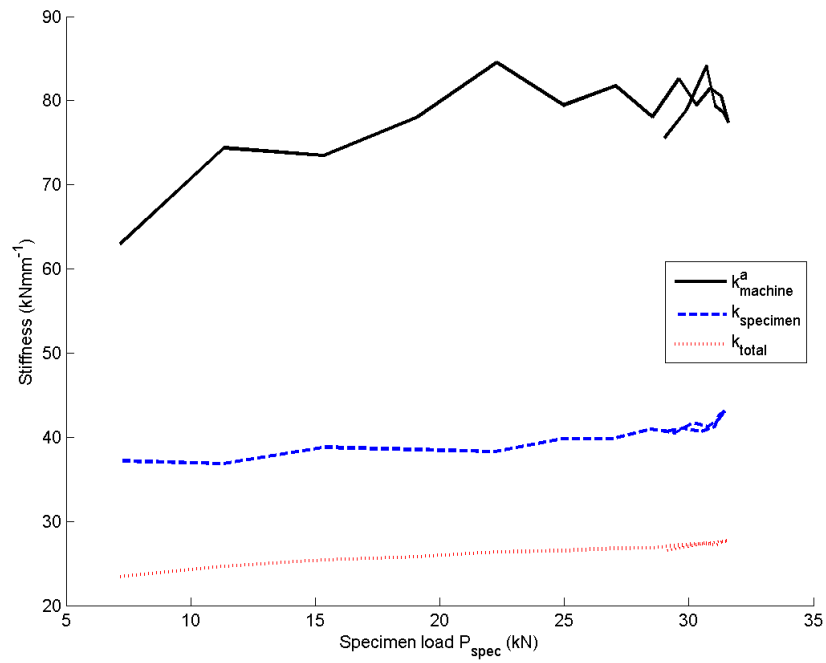


Figure 5.11: Figure comparing stiffness for each unload in 5.10: k_{spec} , calculated from the extensiometer, k_{total} calculated from Instron measurements, and $k^a_{machine}$ inferred from the two using 5.2b

Using data from partial unloads shown in fig. 5.9, it is possible to find $k_{machine}^a$. The gradient of each unload was found from a line of best fit, and the results are plotted in fig. 5.11. On the same plot, k_{total} and k_{spec} are shown. Taking the average of the machine stiffness across all unloads gives a value for $k_{machine}^a$ of 75.2 kNm^{-1} .

In fig. 5.10, an offset from the origin is also observed. This is due to the small gap between the loading pins and the holes of the specimen. When a displacement is first applied to the clevis grips, there is a slight displacement of the pins that does not translate into displacement of the specimen. This displacement has been characterised as $\delta_{bedding}$, and its value is dependent on the relative positions of pins and specimen at the start of a test.

5.3.3 Validating estimates of machine stiffness

Thus far, two estimates of machine stiffness, $k_{machine}^a$ and $k_{machine}^b$ have been made. To validate these values k_{spec} calculated from k_{total} using $k_{machine}$ can be compared against the theoretical value of k_{spec} .

As described in section 5.2.1, theoretical values of k_{spec} from analytical solutions and measurements of k_{total} were found for specimens with three different crack lengths. These values are displayed on a bar chart in fig. 5.12.

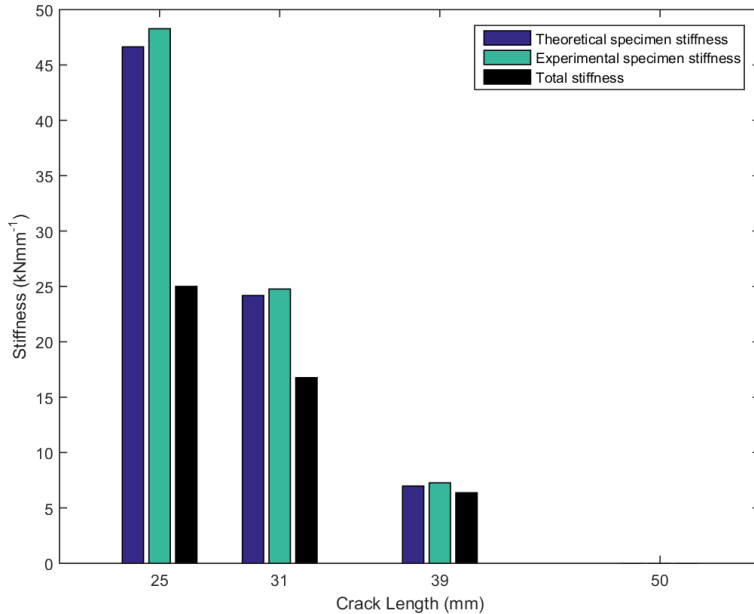


Figure 5.12: A comparison of specimen stiffness at varying crack lengths. Theoretical specimen stiffness is found from the analytical solution (eq. (3.5)) using the measured crack length. Total stiffness, k_{total} , incorporates machine and specimen stiffness. Experimental specimen stiffness is the specimen stiffness found from k_{total} and $k_{machine}$.

On the same chart, values of k_{spec} calculated from $k_{machine}$ and k_{total} for each crack length are shown. For a crack length of 25 mm, k_{total} was measured on the initial load up, thus $k_{machine}^b$ was used to calculate experimental k_{spec} (eq. (5.2b)). For crack lengths of 31 mm and 39 mm,

k_{total} was measured on a partial unload, hence $k_{machine}^a$ was used to calculate experimental k_{spec} . These values of experimental k_{spec} are compared against theoretical values on fig. 5.12.

Fig. 5.12 shows that there is a good correlation between the two measures of k_{spec} . The experimental specimen stiffness (found from k_{total} and $k_{machine}$) is a good match to the theoretical stiffness of the specimen given its crack length. This validates the values of $k_{machine}^a$ and $k_{machine}^b$ obtained from experimental data. Now that the two machine stiffness values have been identified and quantified they may be incorporated into the control algorithm for mechanical testing.

5.4 Displacement mapping

With a value for machine stiffness, it is now possible to convert from k_{total} to k_{spec} . This means that specimen displacement can be known at any time, despite the difficulty of directly measuring it. In the same manner, it is also possible to find a total displacement that will induce the desired specimen displacement. Referring back to fig. 5.10, we can construct a simple formula for machine displacement as a straight elastic line:

$$\delta_{machine} = \frac{P_{spec}}{k_{machine}} + \delta_{bedding} \quad (5.4)$$

where $\delta_{bedding}$ is a constant offset caused by bedding-in effects in the clevis grips and pins. This is given by the x-intercept of the line of best fit in the elastic region of fig. 5.10. Using eq. (5.3), and substituting in eq. (5.4), δ_{total} is given by:

$$\delta_{total} = \delta_{spec} + \frac{P_{spec}}{k_{machine}} + \delta_{bedding} \quad (5.5)$$

here the value of $k_{machine}$ ($k_{machine}^a$ or $k_{machine}^b$) used is dependant on the region that the test is currently in (unloading/reloading or loading up). Similarly, $\delta_{bedding}$ also depends on the $k_{machine}$ chosen, as this will change the x-intercept, as seen in fig. 3.4.

Using eq. (5.5), it is now possible to find specimen displacement at any point during an experiment knowing only total displacement. With specimen displacement, specimen stiffness can be found. By rearranging the relationship in eq. (5.5), it is possible to find the total displacement which will give the desired specimen displacement. This allows accurate experimental results without directly measuring specimen displacement.

In this section, the testing equipment has been modelled to allow for accurate measurements. Incorporating these nuances into the final control algorithm will help to ensure valid results which describe the true behaviour of the specimen under varying loading conditions.

6 Algorithm implementation and validation

The algorithms developed in section 3, which were modified due to testing complications discussed in section 5, were programmed into LabVIEW. The LabVIEW programme was then interfaced with the Instron controller to replicate three bar rig conditions on a C(T) specimen. Initially, tests were carried out in the linear-elastic region to ensure that the basic code was functioning properly. This code was then built on in order to test in the elastic-plastic region. The effects of plasticity and elastic follow-up were looked at in the elastic-plastic region, with particular emphasis on the amount of relaxation of residual stresses as a result of varying levels of elastic follow-up.

6.1 Linear-elastic region

In this section, the results from the linear-elastic mechanical testing are presented. They are in agreement with the theoretical results produced in section 3. The linear-elastic testing serves as ground work on which to build upon into the elastic-plastic region. It is recognised that in the linear-elastic tests, machine compliance from section 5.3 is not accounted for and all values for force, displacement and stiffness are for the machine and specimen in series. This is deemed acceptable as all displacements and forces will be linear in these tests, and so the behaviour of the machine-specimen system is representative of the behaviour of the specimen.

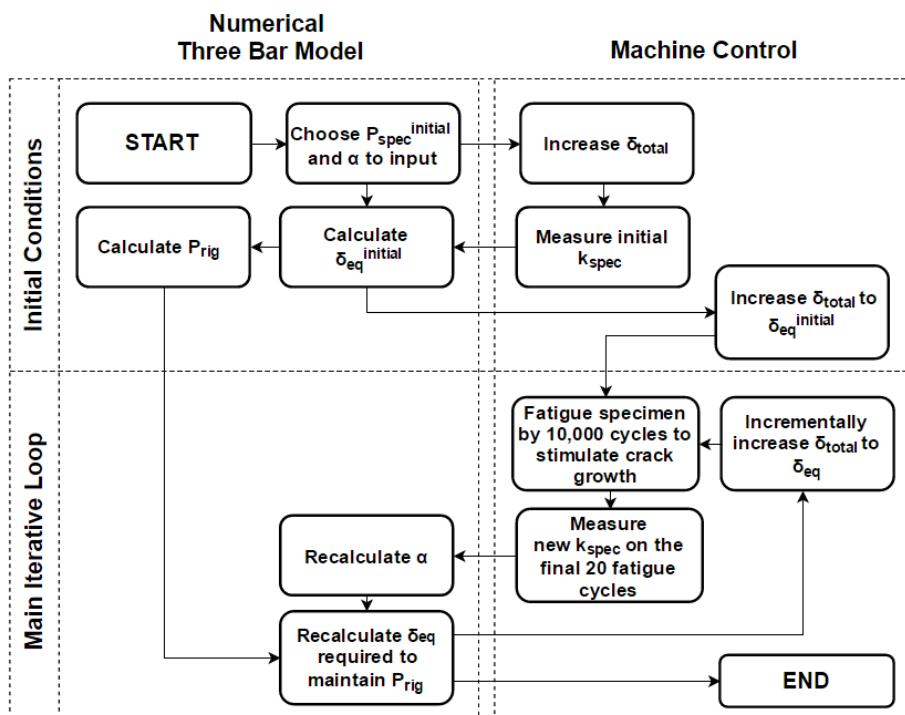


Figure 6.1: Linear-elastic data flow loop

The linear-elastic data flow loop from section 3.2 was modified to incorporate demands sent to and feedback received from a test machine. Processes designed to achieve this have been categorised as machine control in the data loop (fig. 6.1). This is not to be confused

with machine compliance, which will be used in the following sections. The processes involve an initial increase in specimen displacement from which the initial stiffness, k_{spec} , could be measured. Fatigue cycling was used as a method of crack extension, where 10,000 cycles were applied in displacement control about a fixed amplitude of 0.12 mm. The new stiffness was measured by taking an average of the stiffness of the last 10 fatigue cycles. The data flow as shown in fig. 6.1 was transferred into LabVIEW and tested on three specimens, for α values of 1×10^{-9} , 1 and 1×10^9 .

6.1.1 Evaluating algorithm behaviour

From theory discussed in section 3.2, the following results are expected. In fixed-load control, k_{spring} is infinitely more compliant than k_{spec} . Hence, the specimen bears the entire load. As the specimen cracks and k_{spec} decreases, the value of α remains infinitely large. This results in the specimen continuing to bear the entire load. This would manifest graphically as a horizontal line in the load-displacement graph.

Conversely, in fixed-displacement control, k_{spring} is infinitely more stiff than k_{spec} . As the specimen cracks, k_{spec} decreases. Nevertheless, α remains infinitely small. The load shed by the specimen is entirely taken up by the springs. This would manifest graphically as a vertical line in the load-displacement graph.

In finite compliance loading, the change in k_{spec} makes a considerable difference to the value of α . This results in the load shedding between the springs and specimen, and a profile somewhere between displacement and load control. This would manifest graphically as a downward sloping line on the load-displacement graph.

The experimental results are shown in figs. 6.2(a) to 6.2(c), which plot the displacement-load data from the Instron controller. The mean load path, which distinguishes the load path computed by the numerical three bar rig from fatigue data, are the solid lines (black) on the plots. They are in good general agreement with the expected behaviour from numerical simulations shown in fig. 3.2. On all three plots a slight overshoot is observed on the initial load up. This is due to the fact that bedding-in was not accounted for, which led to a smaller stiffness on the initial load up used to calculate $\delta_{eq}^{initial}$. This results in a miscalculation of $\delta_{eq}^{initial}$ to be larger, which causes an overshoot above the selected $P_{spec}^{initial}$. This overshoot is not observed on the subsequent iterations where stiffness were measured from the fatigue cycles, as bedding-in is no longer a factor at higher loads.

In finite compliance control, the mean load path follows a diagonal line as shown in fig. 6.2(a). This result agrees with expected behaviour from the Matlab simulations. Similarly for fixed-displacement control ($\alpha = 1 \times 10^9$), the mean force on the specimen drops almost vertically down as crack growth occurs, close to the value expected, as seen in fig. 6.2(b). The deviation from the vertical axis can be attributed to a small finite compliance effect due to the fact that the specimen is in series with the machine. Smith et al. (2009) asserts that having two elements in series as the central bar will result in never being able to achieve fixed-displacement control - even with an infinitely high value of α . It is believed this effect is the reason why the experimental results for fixed-displacement is not a vertical line down.

The fixed-load control test did not give results entirely as expected. Initially, as seen in fig. 6.2(a), the recalculated values of δ_{spec} after each block of fatigue cycling begin to move horizontally, as predicted from the Matlab model. After 0.75 mm, however, at the onset of plastic deformation, the values fall away from the expected horizontal line. This is due to plasticity occurring in the specimen as a result of elastic-plastic fatiguing. The updated values of δ_{spec} , which LabVIEW calculates based on current stiffness, are much higher than they should be. This is caused by plasticity in the specimen, which is not accounted for at this stage. Hence, the horizontal trend tails off. This trend for fixed-load control testing is also noted in Seow (2015).

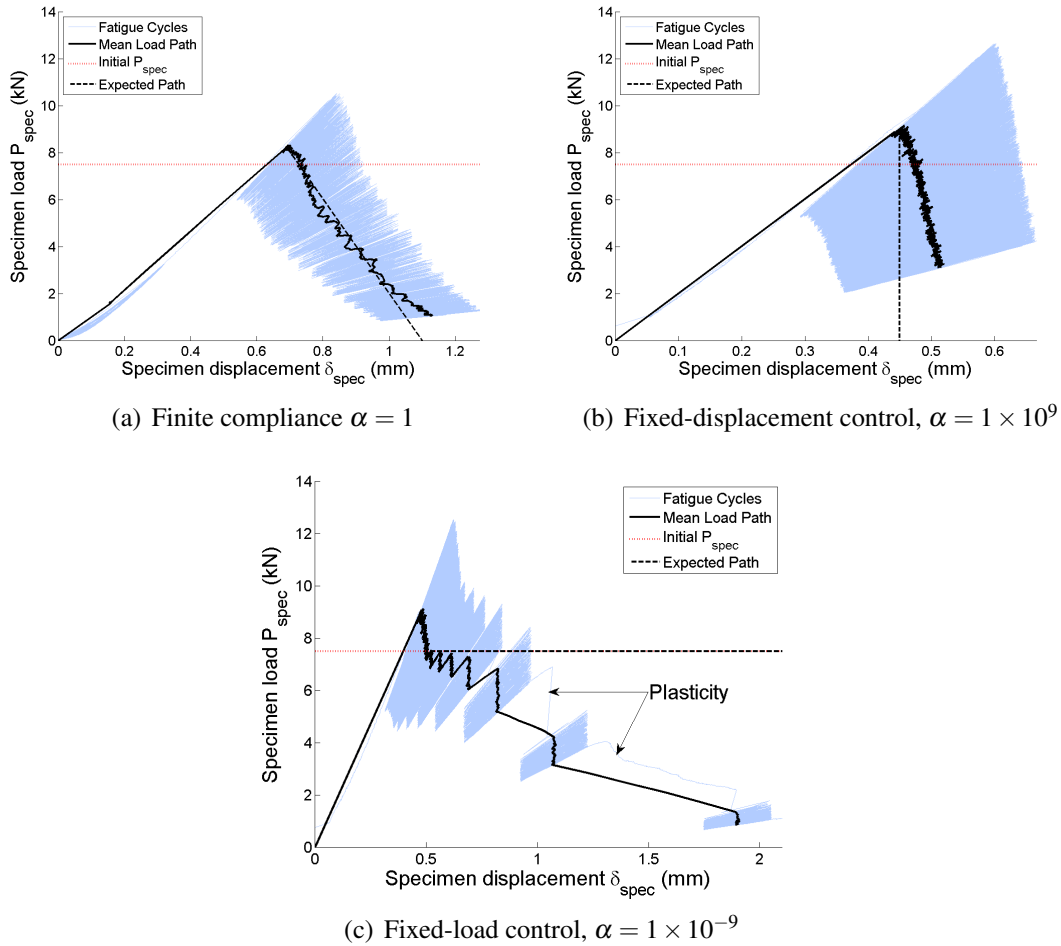


Figure 6.2: LabVIEW linear-elastic testing for a constant P_{rig} . The distribution of P_{rig} between specimen and springs is recalculated based on crack growth. Crack growth is introduced via fatiguing cycling. Solid (light blue) line shows the fatigue cycle. Solid (black) line is the mean force of each load cycle. Dashed line (black) is the predicted behaviour from theory.

6.1.2 Validating LabVIEW algorithm against manual calculations

As seen in section 6.1.1, the accuracy of the algorithm in a mechanical test is affected by bedding-in effects, improvements to the LabVIEW code were made to account for this. Furthermore, ensuring that the algorithm modelled in Matlab is properly transferred and implemented in LabVIEW is critical if it is to be built on into the elastic-plastic region. To this end, two tests

were done to simulate identical loading paths in finite compliance loading conditions. In the first, manual calculations were made and used to adjust the machine inputs on Instron Wavemaker. In the second, all values for the next iteration were calculated by the LabVIEW algorithm and were fed back into the Instron machine. The data are plotted in fig. 6.3.

For the manual calculations, due to the way tests are programmed in Instron Wavemaker, simultaneous measurements of stiffness while the specimen was loaded in the test machine were technically challenging to make. Therefore, an initial stiffness measurement and $\delta_{bedding}$ calculation had to be made before the start of the tests and in between iterations (i.e. in between blocks of fatigue cycling). The stiffness measurements were made above a load of 2 kN to avoid inaccuracies due to bedding-in, and the starting position was kept the same to keep bedding-in constant for each iteration. With a value for initial stiffness, a $P_{spec}^{initial}$ of 14 kN was selected, from which the corresponding $\delta_{eq}^{initial}$ was calculated. Using Instron Wavemaker, a displacement equal to the sum of $\delta_{eq}^{initial}$ and $\delta_{bedding}$ was applied to the specimen. 10,000 fatigue cycles were applied about this displacement at an amplitude of 0.12 mm. After which the specimen was fully unloaded in order to export the data, from which the stiffness of the last 20 fatigue cycles were measured. An average was taken and this new stiffness was used to recalculate δ_{eq} . The next iteration begins, where a displacement equal to the sum of recalculated δ_{eq} and $\delta_{bedding}$ is applied to the specimen using Instron Wavemaker. The iterations continued in this vein.

The results from the manual calculations are shown in fig. 6.3(a). By accounting for $\delta_{bedding}$, the overshoots on the initial load up have been eliminated. This method used to account for $\delta_{bedding}$ was hence transferred to the LabVIEW algorithm, which was subsequently tested with the same $P_{spec}^{initial}$ of 14 kN. In the LabVIEW environment, as the specimen stiffness could be measured simultaneously while a displacement was applied to the specimen, the iterations were ran continuously. The results are shown in fig. 6.3(b).

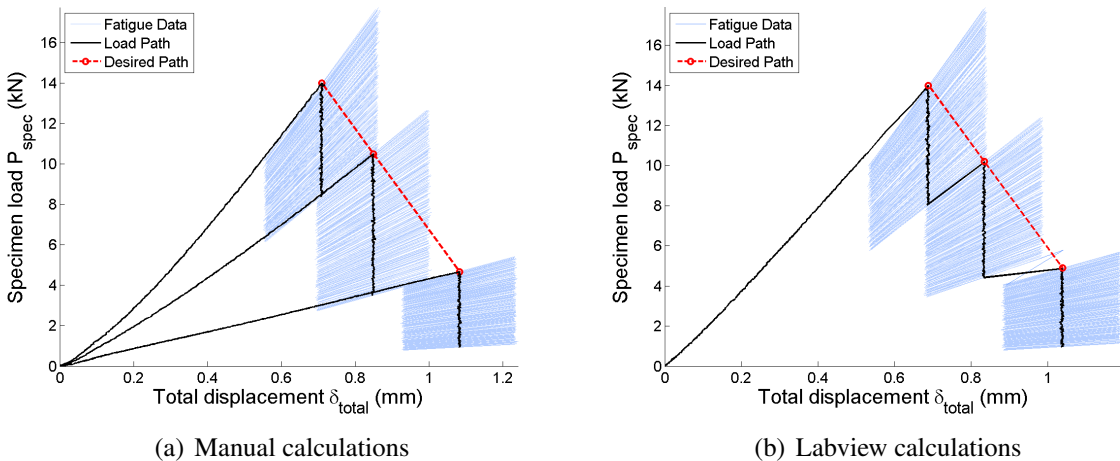


Figure 6.3: Comparison of load vs machine displacement results for calculations done manually and by LabVIEW

There is good agreement between the results from the LabVIEW and manual calculations. The dashed line (red) which lines up the points to which the second and third iterations were loaded up to, are identical and agree with the Matlab simulation. Fig. 6.4 plots the specimen

stiffness in the two tests against each other. Identical stiffness evolution through the tests would give a diagonal line at 45° anticlockwise from the x-axis, shown by a dashed (black) line. The actual stiffness comparison has small deviations from the idealised behaviour but still shows excellent agreement between the two tests.

This indicates that the algorithm has been accurately implemented in LabVIEW. The LabVIEW model can now be used for testing in the linear-elastic region and extended to account for plasticity and residual stresses in the elastic-plastic region.

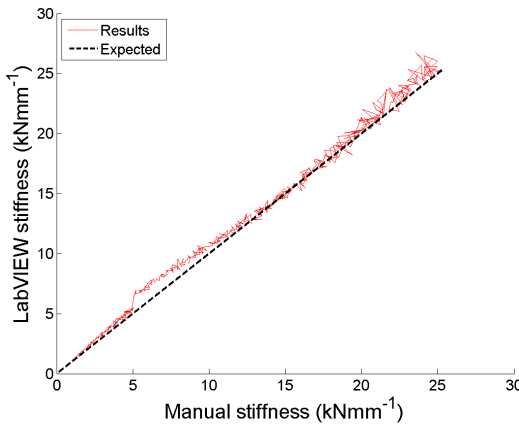


Figure 6.4: Comparison of stiffness for calculations done manually and by LabVIEW. Ideally the solid red results line would match the solid black line of gradient one, indicating both sets of stiffness are identical.

In this section the theory for the linear-elastic region which was demonstrated in Matlab has now been transferred into LabVIEW. The results from the LabVIEW testing for all three loading conditions shows good consistency with theory, with exception to fixed-load control, where plasticity had an effect on the tests. The effects of plasticity will have to be taken into consideration when extending the theory into the elastic-plastic region.

6.2 Elastic-plastic region

With confidence in the algorithm, gained from testing in the linear-elastic region, it was developed for the elastic-plastic testing. The effects of elastic follow-up and plasticity on residual stress relaxation as described in section 3.3 were accounted for according to the data flow in section 3.3.2. The processes used to extract data from the EPRI solutions were replaced with machine controls, which translate computations into machine demand. The effects from bedding-in were accounted for using the methods described in section 6.1.2.

Furthermore, in order to obtain accurate readings of specimen stiffness and plastic deformation, machine compliance must be incorporated into the algorithm. The two methods have been adopted to achieve this. The first method involves mapping one measured stiffness onto the other using a stiffness correction factor, CF, and is described in section 6.2.2. The experimental results and discussions from this method are also presented here. The second method described in section 6.2.3 is a full implementation of machine compliance, which translates both

measurements of stiffness into specimen stiffness. The final data flow with full implementation of machine compliance used for testing in the elastic-plastic region is shown in fig. 6.8. The experimental results from testing the final LabVIEW algorithm are also presented in section 6.2.3, followed by a discussion of these results in section 6.2.4.

For both methods, results for the three loading conditions; finite compliance, fixed-load and fixed-displacement control approximations are shown. The α values used are 1, 1×10^{-9} and 1×10^9 respectively.

6.2.1 Incorporating machine compliance

The algorithm thus far comprises two domains, numerical three bar model and machine control. The former computes values of variables used in the theoretical three bar model, the latter translates these variables into machine demand. Inversely, the machine control domain receives measurements from the test machine and translates them into values appropriate for the numerical three bar model. When there is sufficient machine compliance acting between the two domains, the values sent between them are no longer equal and this difference must be accounted for.

As described in section 5.3.1, measurements from the Instron controller gives total stiffness, k_{total} , which is given by eq. (5.2). In order to accommodate the two values of machine stiffness, two new variables, k_{total}^a and k_{total}^b , were defined and are given by:

$$k_{total}^a = \left(\frac{1}{k_{machine}^a} + \frac{1}{k_{spec}} \right)^{-1} \quad (6.1a)$$

$$k_{total}^b = \left(\frac{1}{k_{machine}^b} + \frac{1}{k_{spec}} \right)^{-1} \quad (6.1b)$$

where $k_{machine}^a$ and $k_{machine}^b$ are the values of machine stiffness on the partial unload and initial load up respectively. For clarity, k_{total}^a and k_{total}^b are marked out on a load-displacement graph in fig. 6.5.

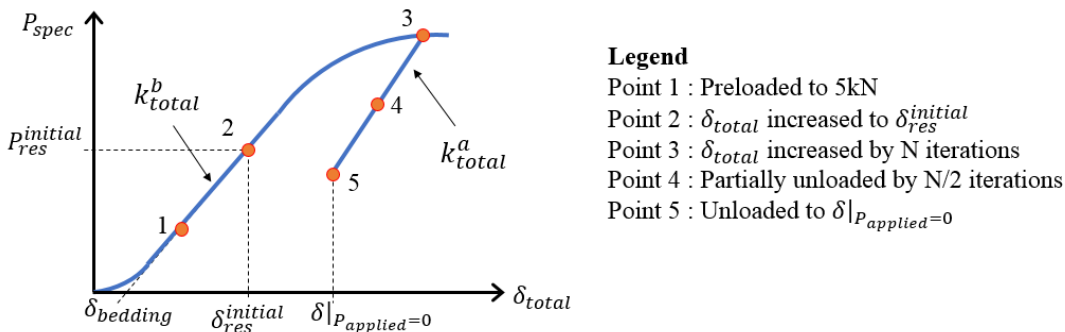


Figure 6.5: Highlight of key steps in the LabVIEW algorithm used in section 6.2.2 and section 6.2.3 on a load-displacement graph.

Displacement demands to and measurements from the machine are defined as δ_{total} as seen in eq. (5.5). A measurement of $\delta_{bedding}$ was made by applying a pre-load of 5 kN above which the initial stiffness measurement was taken. This ensured that the stiffness measured on the load up was not affected by the bedding-in of the loading pins. A summary of the key processes in the algorithm are shown in fig. 6.5.

6.2.2 Partial implementation of machine dynamics with a stiffness correction factor

As a first step towards full implementation of the machine compliance into the system, a partial implementation was done. The partial implementation of machine compliance utilised machine stiffness values, acquired in section 5.3, to map stiffness measurements of the unload onto those of the initial load up. In effect, the partial implementation removed the ramifications of the dependency of $k_{machine}$ on the part of the loading cycle i.e. consolidates $k_{machine}^a$ and $k_{machine}^b$ into one correction factor. Using this correction factor allowed the evolution of residual stress to be characterised in terms of δ_{total} rather than δ_{spec} . By rearranging eq. (6.1), the total stiffness measured on the unload, k_{total}^a , can be mapped onto the total stiffness measured on the original load up k_{total}^b using:

$$k_{total}^b = \frac{k_{total}^a}{1 + CF k_{total}^a} \quad (6.2)$$

where the stiffness correction factor, CF , is

$$CF = \frac{k_{machine}^a - k_{machine}^b}{k_{machine}^a k_{machine}^b} \quad (6.3)$$

To include the stiffness mapping, a stiffness correction factor domain was implemented into the Matlab algorithm as a layer in between the numerical three bar model and the machine control domain. It is important to note that the steps in the numerical three bar rig as seen in fig. 6.6, has remained the same throughout the development of the algorithm for the elastic plastic region.

In the stiffness correction domain, $\delta_{bedding}$ is calculated from an initial stiffness measurement, k_{total}^b . This is then added to the initial δ_{res} calculated in the numerical three bar model. This is set as the machine demand and sent to the test machine via the machine control domain. After a partial unload, the stiffness correction factor, CF , is applied to the stiffness measurement obtained, k_{total}^a . This maps k_{total}^a onto k_{total}^b . k_{total}^b is then fed into the numerical three bar model, where $\delta|_{P_{applied}=0}$ is calculated. In order to translate this value into machine demand, $\delta_{bedding}$ is added, then sent to the machine control domain. A demand signal is sent from this point to the test machine to unload to the desired displacement, and the feedback loop carries on in an iterative manner. This flow is illustrated in fig. 6.6.

This method was tested experimentally with a simulated residual load of 7 kN. The results are shown in fig. 6.7 and they demonstrate good general agreement with the Matlab simulation described in section 3. The dot-dashed (black) lines show how the residual load was predicted to evolve with plastic deformation. The solid-o (red) lines show the residual load path in the

specimen, and the dashed (blue) lines show the total load path of the specimen.

The fixed-displacement control results in fig. 6.7(a) show a very good agreement with the prediction. However, the results from the finite compliance and fixed-load control tests (figs. 6.7(b) and 6.7(c)) show that the full unload to $\delta|P_{applied} = 0$ consistently undershoots. This indicates that the algorithm is calculating a larger $\delta|P_{applied} = 0$ than required. This could be due to the fact that whilst the algorithm calculates $\delta|P_{applied} = 0$ using a smaller mapped stiffness k_{total}^b , but the specimen continues to unload along the larger k_{total}^a . Another factor could be small inaccuracies in stiffness measurements on the partial unloads.

The fixed-displacement control results show a better agreement with the Matlab codes than the other two alpha conditions because in fix-displacement control, the displacement to which the specimen is unloaded to, $\delta|P_{applied} = 0$ is not dependent on plasticity. The remaining residual load however, will be affected by plasticity, and the effects of the stiffness measurements manifests in a difference in P_{res} instead of a difference in $\delta|P_{applied} = 0$.

The reasons for the slight discrepancy in the experimental and predicted results were not thoroughly investigated as the data represents the behaviour of a specimen with a spring in series and not the specimen itself. The good general agreement however provides assurance that machine compliance has been mostly accounted for. This led to the implementation of the final LabVIEW code, which translates the measured data into specimen data.

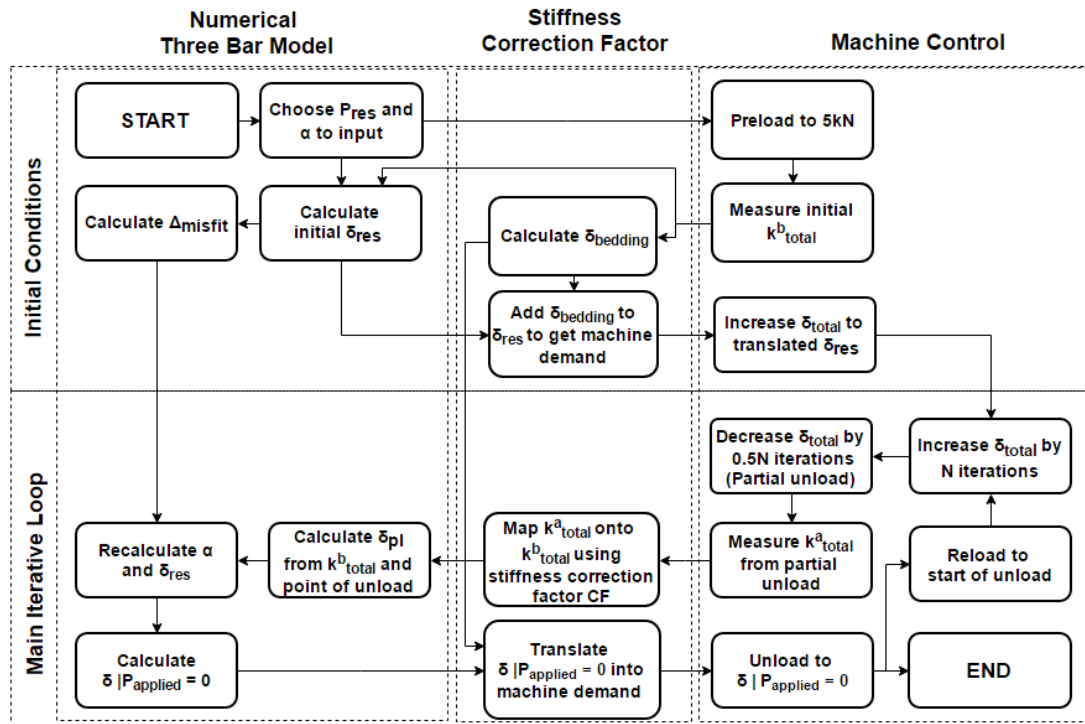


Figure 6.6: Data flow loop for the LabVIEW algorithm with the stiffness correction factor.

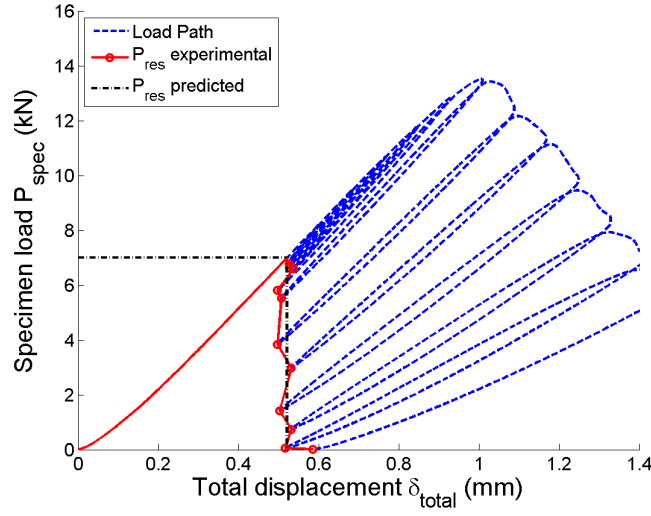
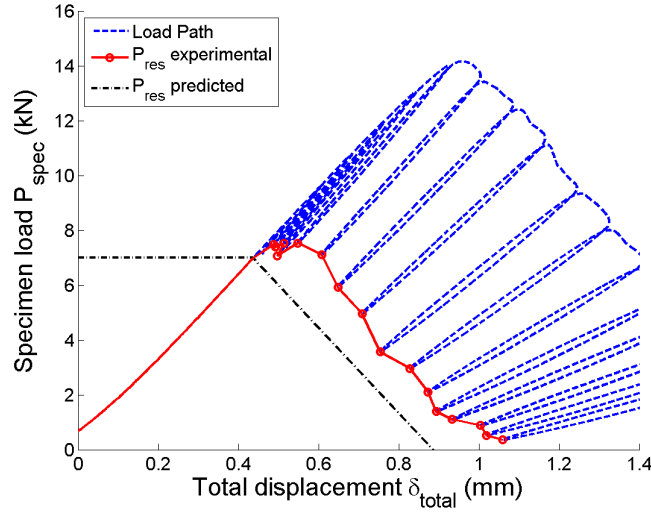
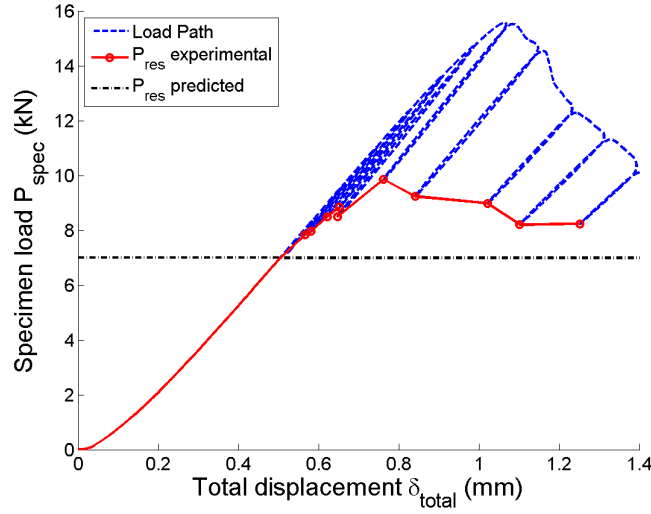
(a) Fixed-displacement control, $\alpha = 1 \times 10^9$ (b) Finite compliance $\alpha = 1$ (c) Fixed-load control, $\alpha = 1 \times 10^{-9}$

Figure 6.7: The experimental results for the relaxation of P_{res} as plasticity increases for the three loading conditions.

6.2.3 Full implementation of machine dynamics

In the previous section, where partial implementation of stiffness mapping was made, all the values of machine compliance are combined into one value to ensure consistent results. It is still only possible for to plot data for specimen and machine in series to be plotted. In this section, machine compliance is completely accounted for. This allows specimen data to be plotted.

The final implementation of machine compliance involved translating the measurements of k_{total}^a and k_{total}^b obtained from the machine measurements, into specimen stiffness, k_{spec} , using eq. (6.1). This is done in the machine compliance mapping domain shown in fig. 6.8. The value of k_{spec} is then fed into the numerical three bar model, where the same algorithm from section 3.3.2 computes values of $\delta_{res}^{initial}$, δ_{pl} , δ_{res} and $\delta|P_{applied=0}$. From the numerical model, $\delta|P_{applied=0}$ is sent to the machine compliance mapping domain, where it is translated into machine demand via $k_{machine}^a$. This value of displacement demand is sent to the machine control domain, which is subsequently sent as a voltage signal to the test machine. The steps in the numerical three bar model and machine control domains remain the same as before.

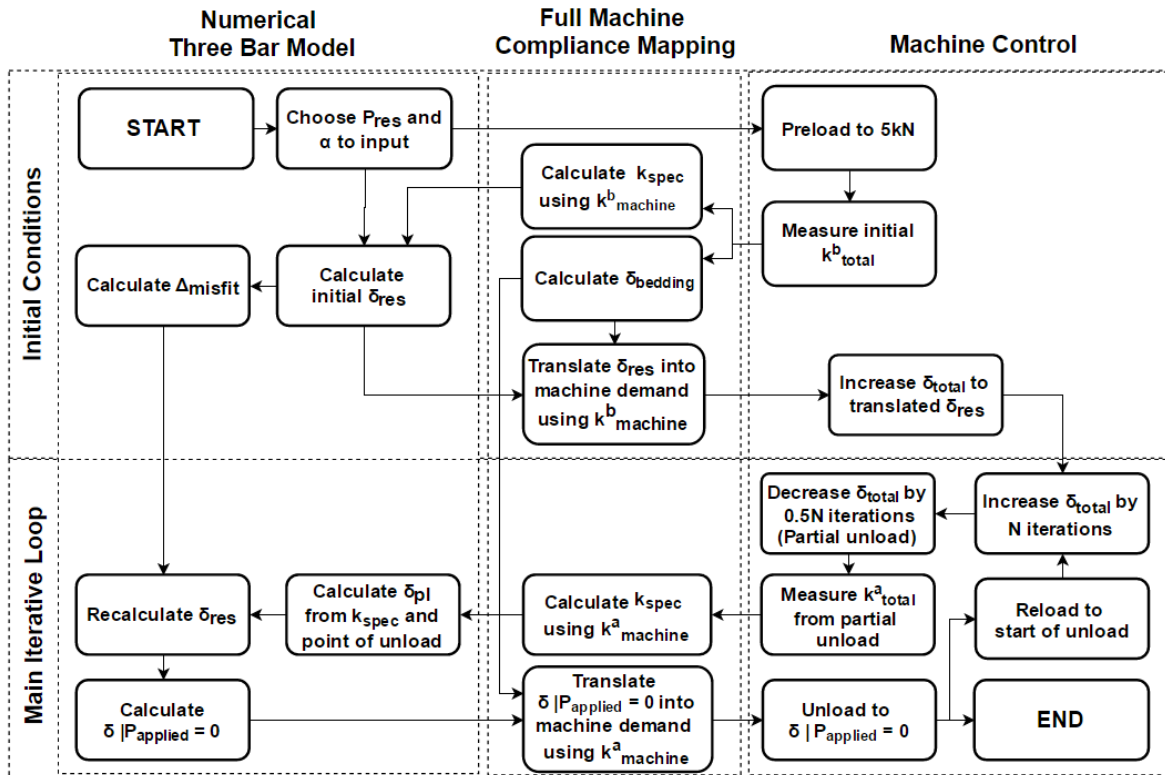


Figure 6.8: LabVIEW elastic-plastic data flow loop with steps categorised into three domains, the numerical three bar model, machine compliance mapping, and machine control. The first domain contains the numerical calculations based on the equations from the theoretical three bar model, the second translates inputs and outputs from the first and the third using machine compliance, and the third domain sends demand signals to the test machine.

Fig. 6.9 shows the experimental results from the LabVIEW algorithm with full implementation of machine compliance. The total displacement as measured by the Instron controller is shown by the dashed lines (black). Using values of $k_{machine}$ obtained from section 5.3, these data were translated into specimen displacement. Both sets of data are plotted on the same graphs in solid lines (blue). The difference between the total displacement and specimen displacement in the results highlights the importance of including machine dynamics.

The endpoints of the unloads represent the evolution of residual stress as plasticity increases when the applied loading is completely removed. The endpoints of the unloads for the specimen load path in fig. 6.9 show a good general agreement with the Matlab simulation described in section 3.3.3. For fixed-displacement control, residual load is expected to decrease with no change in specimen displacement and the endpoints of the unloads should line up on a vertical line. This is observed to a large degree of accuracy on the specimen load path in fig. 6.9(a).

For finite compliance control, the residual load is expected to drop with increasing amounts of plasticity and the endpoints should line up on a linear diagonal line. A slight deviation from this prediction is observed on the specimen load path in fig. 6.9(b). For fixed-load control, the residual load is expected to remain constant as plasticity increases. Again, a deviation from this prediction is observed on the specimen load path in fig. 6.9(c). The reasons for these discrepancies are investigated in section 6.2.4.

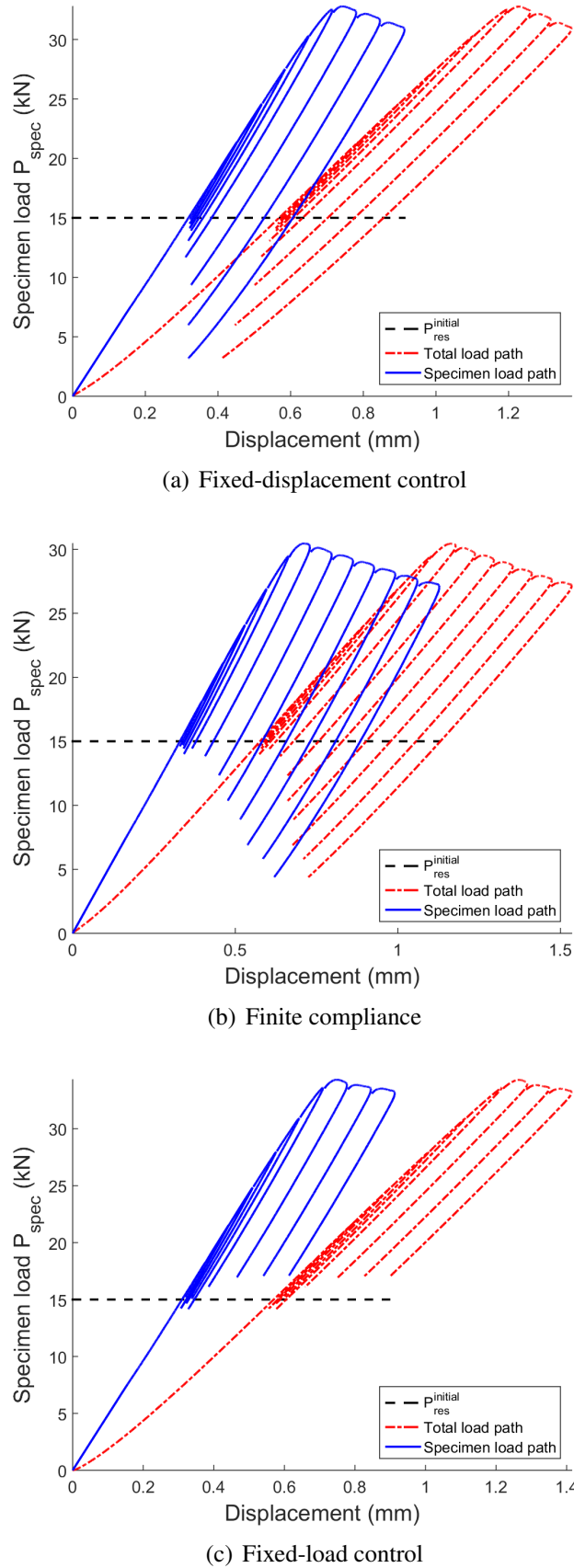


Figure 6.9: Three α conditions with residual load of 15 kN. The dot-dashed (black) line shows is for the total values of displacement for specimen and machine in series, δ_{total} . Solid (blue) lines show the δ_{spec} calculated from δ_{total} based on machine dynamics.

The experimental data was post processed in Matlab to simulate the development of residual stress when the applied force increases. The results are shown in fig. 6.10. The development of residual stress and applied load comprise to produce the total load on the specimen in each loading condition. In each case, residual stress in the specimen remains relatively constant while the specimen is still loaded in the linear-elastic region. After the onset of plasticity, the relaxation rate of residual stress varies for the different values of α . In fixed-displacement control, the residual stress in the specimen dropped off considerably. The residual stress diminished at a reduced rate in finite compliance loading. In fixed-load control, the residual load remains constant in spite of plasticity. All three graphs follow similar trends to those in fig. 3.7 produced from eqs. (3.15) and EPRI solutions as described in section 3.3.3.

The primary difference between the EPRI solutions and the mechanical testing conducted is that the perfectly elastic-plastic load path predicted by the EPRI solutions does not take into consideration crack growth. Crack growth is evident in the experimental results after 0.7 mm specimen displacement. At this point, the load begins to tail off as specimen stiffness reduces. Whilst this suggests that it is likely that crack growth will cause the residual load to decrease further, it is not clear from the experimental results the true effects of crack growth on the evolution of residual stress in the specimen. Furthermore, the deviations from the simulations could be attributed to experimental factors, which are discussed in section 6.2.4.

However, the fact that the control algorithm does take into account both plasticity and crack growth to produce experimental results with expected trends opens up new possibilities in the study of the effects of crack growth on residual stress in finite compliance load conditions.

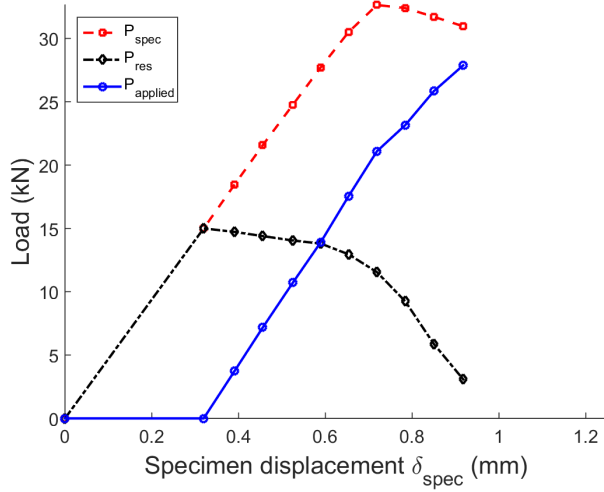
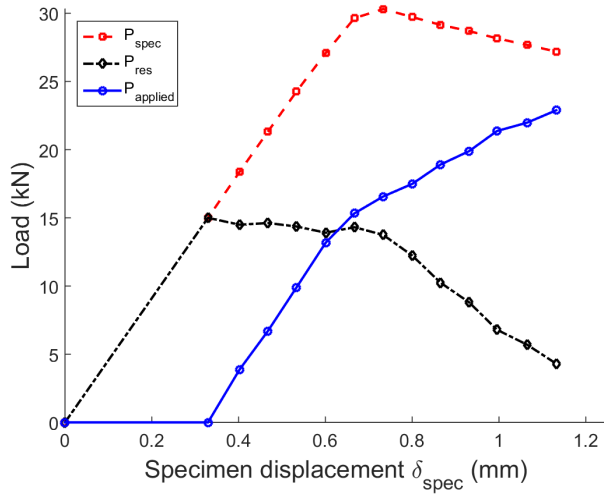
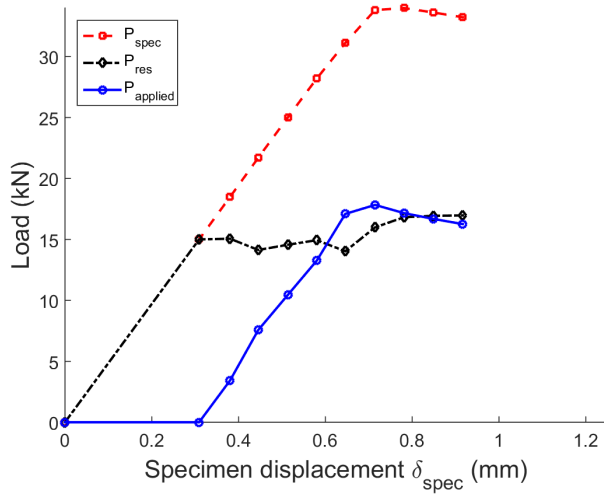
(a) Fixed-displacement control, $\alpha = 1 \times 10^9$ (b) Finite compliance $\alpha = 1$ (c) Fixed-load control, $\alpha = 1 \times 10^{-9}$

Figure 6.10: The three alpha conditions, showing the development load with displacement. Specimen load P_{Spec} from the experiment is displayed, as well as its constituent residual and applied loads as calculated by the controller.

6.2.4 Experimental stiffness measurements from partial unloads

As described in section 6.2.3, the finite compliance and fixed-load control results deviate slightly from the simulations. This suggests that there may have been discrepancies in the calculation of the displacement $\delta|_{P_{applied}=0}$, given by eq. (3.15). As $\delta_{res}^{initial}$ is a constant, the only factor which could be affecting this calculation is δ_{pl} , which value is dependent on the stiffness measured on the partial unload. Upon further investigation, it was found that the stiffness of the specimen varied with the length of the unload. Using the data from the fixed-load control test, the gradient of the partial unloads were plotted against the index of blocks of 20 data points on the unload, as shown in fig. 6.11. The indexing begins from the start of the unload.

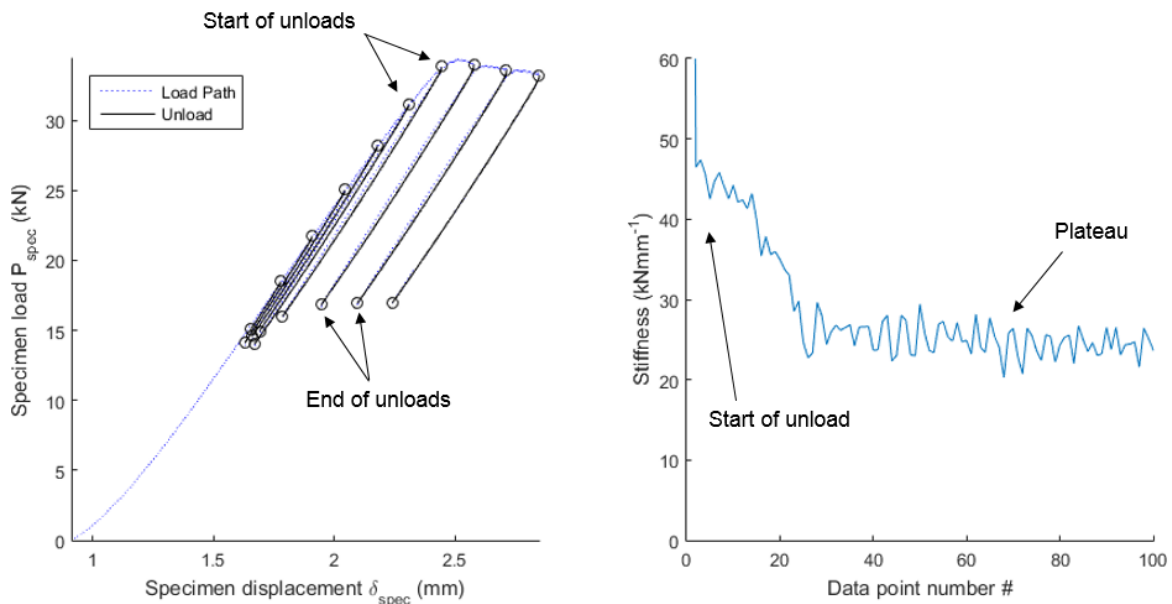


Figure 6.11: Figure demonstrating the variation in stiffness measured from the unloads. Left: Plot of load-displacement data. Right: Plot of the stiffness measured from an unload against the index of blocks of 20 data points on the unload. Note the higher value of stiffness at the start of the unload, and the lower plateau. Similar trends were observed for all the unloads.

It can be observed that the main body of the unload has a significantly lower gradient than the start of the unload. At the top of the unload, there is a very large gradient, but after the 30th block of data points, the gradient of the unloads remains relatively constant. This shows that there is a minimum size of the partial unload which must be made in order to get an accurate stiffness reading, which is calculated to be in the region of 2 mm.

The gradient at the start of the unload was used as the specimen stiffness measurement during the LabVIEW testing, which means that the stiffness values sent into the numerical three bar model was higher than desired. A greater value of specimen stiffness resulted in the miscalculation of a larger δ_{pl} .

As a result, in the fixed-load control LabVIEW test, $\delta|_{P_{applied}=0}$ was calculated to be larger than it should be. Hence, as the controller performs the full unload to $\delta|_{P_{applied}=0}$, unloading is stopped prematurely and the specimen's load-displacement ends up higher on the unload line. This makes it appear as though P_{res} is increasing, when in reality the unloads were stopped

before they should have been. This effect is also observed in the finite compliance control test, albeit to a smaller extent.

In fixed-displacement control, it seems as though the miscalculation of $\delta_{plastic}$ does not affect the results. This is because as shown in eq. (3.17b), $\delta|_{P_{applied}=0}$ is only dependent on $\delta_{res}^{initial}$, which is a constant. The remaining residual load however, will be affected by plasticity, and the effects of the stiffness measurements manifests in a difference in P_{res} instead of a difference in $\delta|_{P_{applied}=0}$.

In order to improve the LabVIEW testing, taking stiffness readings from the main body of the unload would render more accurate values of $\delta|_{P_{applied}=0}$ to unload to. To confirm that this misreading of k_{spec} is the reason for the unexpected results, a Matlab script was written to take the experimental data and read off a gradient from further down the partial unload. This reading for k_{spec} was then used to calculate a value for $\delta|_{P_{applied}=0}$. Figs. 12(a) - 12(c) show the results of taking a more accurate measure of k_{spec} for each loading condition.

Also shown in solid-o (red) lines are the endpoints of the unloads, representing residual stress as plasticity increases.

In each case, the simulated results which read the correct stiffness reading from the unloads are in closer agreement to the theory as laid out in section 3. This confirms that the reason that the fixed-load control and finite compliance unloads were not unloading to the correct $\delta|_{P_{applied}=0}$ is that the stiffness of the unloads was not being measured correctly by the algorithm.

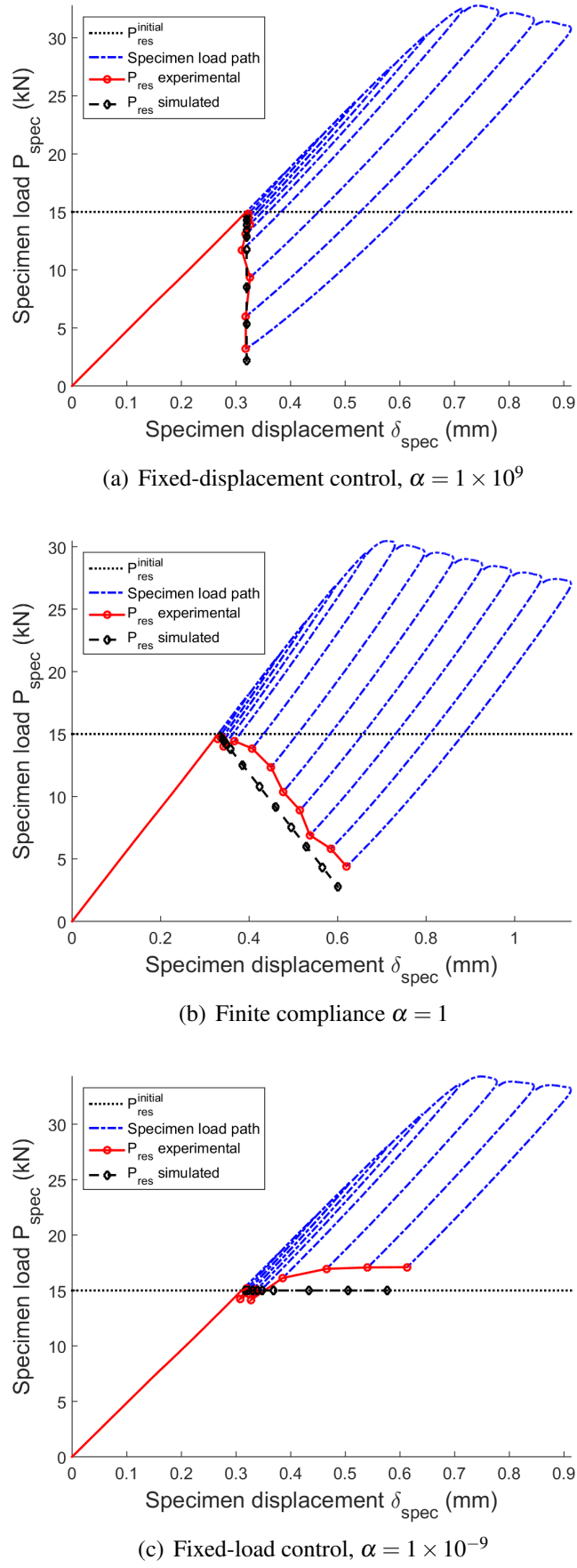


Figure 6.12: The experimental (o) and simulated (\diamond) results for P_{res} for the three loading conditions.

7 Conclusion

Overall, the research presented in this report proves the viability of control feedback as an alternative to the use of a physical three bar rig. It has been shown that it is possible to decouple and measure specimen stiffness and plasticity from periodic unloads. It has also been demonstrated that it is possible to use these measurements in a software controller to accurately replicate the behaviour of a three bar rig in real time.

Within the linear-elastic region, the control loop is able to implement fully fixed-load, fixed-displacement control and finite compliance conditions. Experiments in section 6.1.1 have validated the correct trends under these conditions. Comparison with manual calculations further confirms the correct implementation of the algorithms discussed in section 3.

The effects of machine dynamics are neglected in the linear-elastic region as the behaviour of both machine and specimen will be linear. This gives good assurance that the behaviour of the machine and specimen in series will be representative of the specimen behaviour.

Extension of the controller into the elastic-plastic region is achieved. In the elastic-plastic region, the effects of machine dynamics had to be considered. Highly non-linear machine dynamics were characterised and incorporated into the control algorithm through the use of stiffness mapping of the unload stiffness onto the main machine stiffness. This partial implementation of machine dynamics demonstrated that the correct trends are still observed even when plasticity occurs. The incorporation of a misfit between specimen and spring, and the evolution of residual stresses is also correctly modelled and observed in section 6.2.2.

While this partial implementation of machine dynamics gives correct trends of results, the data acquired is for specimen load vs total displacement. In order to see the behaviour of the specimen alone, the effects of machine dynamics must be completely accounted for. This is done in 6.2.3 with expected results.

Issues with stiffness measurements have been assessed in section 6.2.4. It is found that the stiffness of the specimen must be read from the main body of the unload to render good results. This infers that there is a minimum size of an unload which must be made to effectively decouple crack growth and plasticity.

The final feedback control system with full machine dynamics implemented has enabled fixed-load, fixed-displacement or finite compliance conditions to be induced on the specimen itself. Albeit with some oversight in experimental factors, this system has been tested in the three loading conditions in section 6.2.3.

The accurate measurement of specimen displacement has proven more challenging than expected. The method described in section 5.4, of deriving specimen displacement from total displacement of the Instron machine, has not yet been fully validated with a comparison to an independent measurement of specimen displacement. It may prove to be too heavily reliant on the predictability of machine dynamics. This difficulty could be avoided with a method of directly measuring specimen displacement, a concept discussed in further work.

In summary, this report concludes that feedback control loops are a feasible and useful way of simulating mechanical testing of a three bar system, and should be viewed as a viable replacement for physical rigs.

8 Future work

In addition to addressing the limitations of the set-up and algorithm discussed in section 7, there is opportunity to build on this project with further work. In particular, this method could be expanded on into more complex scenarios and geometries.

8.1 Improving methods for finding specimen stiffness

There are some improvements that need to be made to the algorithm. Firstly, validation of the results found in section 6.2.1. This could be done by comparing the results of from the tests with an independent measure of specimen displacement, found using a video extensiometer in section 4.4.

Secondly, perfecting methods of providing accurate measurements of specimen displacement to the controller. Currently, this is performed using total displacement and factoring out machine dynamics, as shown in section 5.4. One possible area for improvement would be further profiling machine dynamics to improve displacement mapping.

Alternatively, a method of controlling the machine using a direct measure of specimen displacement would bypass the complications caused by the machine compliance. One possibility is using a video extensiometer, which could be connected to the Instron 8800 controller, allowing a value for specimen displacement to be read directly. One limitation with this method, however, is excessive noise in the measurements of the video extensiometer.

8.2 Increasing complexity of loading conditions

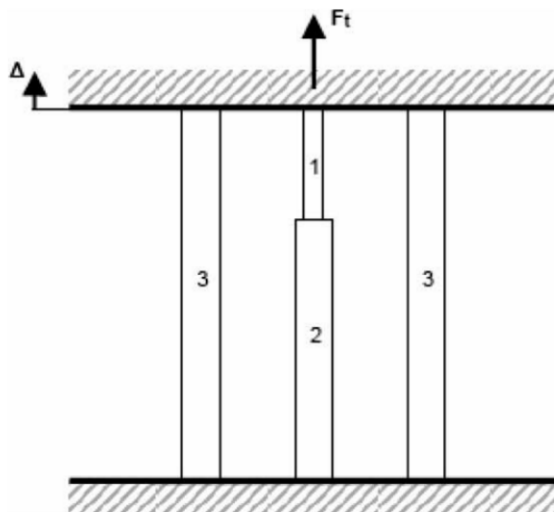


Figure 8.1: Three bar model with two central bars in series (Smith et al., 2009).

The feedback controller concept could be adapted to a wide variety of loading scenarios. For example, the machine stiffness in series with the specimen could be modelled in a different manner. In Smith et al. (2009), the physical three bar model tested was modelled with two

central bars of the same material in series. The difference in cross-sectional area gives the two central bars different stiffness. This set-up is shown in fig. 8.1.

This means that the elastic follow-up factor for three parallel bars, Z_p , is adjusted by an elastic follow-up factor determined by the two central bars in series, Z_s . Thus the combined elastic follow-up factor, Z_c is given by:

$$Z_c = Z_p Z_s = \left(\frac{1+\alpha}{\alpha} \right) \left(\frac{1+\beta}{\beta} \right)$$

where α is the relative stiffness of the outer and inner bars and β is the relative stiffness of the two central bars. This can easily be incorporated into a LabVIEW control algorithm.

Asymmetric loading of the rig could also be considered. Fig. 8.2 gives an example of possible asymmetrical loading which could be applied where $d_1 \neq d_2$.

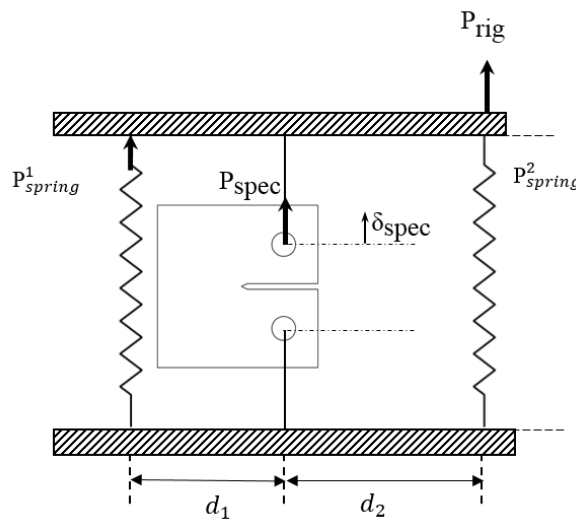


Figure 8.2: An example of asymmetric loading conditions.

This would result in the the force being shared between the specimen and the springs dependent on their relative stiffness and also a geometric factor. This geometric factor would be a function of the distance from the spring (or specimen) in question to the point where the force is applied. It is expected that this would have a significant effect on elastic follow-up and the relaxation of residual stresses.

References

- C. J. Aird. *The influence of long-range residual stress on the cleavage fracture of ferritic steel.* PhD thesis, University of Bristol, England, 2009.
- M. Alfano, L. Pagnotta, and G. Stigliano. Elastic properties of cold rolled aluminium plates with irregular shape by dynamic testing. In *EngOpt 2008 – International Conference on Engineering Optimization*, 2008.
- T. Anderson. *Fracture Mechanics: Fundamentals and Applications, Third Edition.* CRC Press, 2005. ISBN 9781420058215. URL <https://books.google.co.uk/books?id=C5fMBQAAQBAJ>.
- ASTM International. Standard test method for linear-elastic plane-strain fracture toughness K_{Ic} of metallic materials. *E399 – 12e3*, 03(01):18–20, 2013.
- Z. P. Bazant and E. Becq-Giraudon. Effects of size and slenderness on ductility of fracturing strictures. *Journal of engineering mechanics*, 1999.
- J. T. Boyle. A re-assessment of elastic follow-up in high temperature piping. *International Journal of Pressure Vessels and Piping*, 108:7–12, 2013.
- G. Chell. Incorporation of residual and thermal stresses in elastic-plastic fracture mechanics design. In *Joint research centre for the joint European communities*, 1979.
- D. Green and J. Knowles. The treatment of residual stress in fracture assessment of pressure vessels. *Journal of Pressure Vessel Technology*, 1994.
- S. Hadidi-Moud, A. H. Mahmoudi, C. E. Truman, and D. J. Smith. Combined effect of residual stress and loading history on brittle fracture. In *9th International Conference on Mechanical Behaviour of Materials*, 2003.
- G. C. M. Horne. *Elastic follow-up and the interaction between applied and residual stresses.* PhD thesis, University of Bristol, England, 2013.
- Instron CMOD. Crack opening displacement (cod) gauge 10/4, 2016. URL www.instron.co.uk/en-gb/products/testing-accessories/extensometers.
- Instron Wavemaker. Wavemaker cyclic software operator's course, 2016. URL <http://www.instron.us/en-us/service-and-support/training>.
- V. Kumar, M. German, and W. Wikening. Advances in elastic-plastic fracture analysis. *Rep. EPRI/Electric power research inst.*, 1984.
- A. H. Mahmoudi, S. Hadidi-Moud, C. E. Truman, and D. J. Smith. A numerical and experimental investigation into the generation of residual stress in fracture specimens using local compression. In *15th European Conference on Fracture*, 2003.

- W. A. Meith, M. R. Hill, and T. L. Panontin. Analytical and experimental study of fracture in bend specimens subjected to local compression. In *Fatigue & Fracture Mechanics: 33rd Volume*. ASTM International, 2003.
- I. Milne, R. A. Ainsworth, A. R. Dowling, and A. T. Stewart. Nuclear electric procedure r6 revision 3. *International journal of pressure vessel piping*, 1988.
- A. Mirzaee-Sisan. *The influence of prior thermal and mechanical loading on fracture*. PhD thesis, University of Bristol, England, 2005.
- National Instruments Corporation. NI LabVIEW application areas, 2015. URL <http://www.ni.com/labview/applications/>.
- R. Ogeman. Residual stresses and crack propagation after coining of holes in aluminium plates; finite element calculations and verifying experiments. *Transactions on Engineering Sciences*, 1993.
- E. L. Robinson and N. Y. Schenectady. Steam pipe design to minimize creep concentrations. *Transactions of the ASME*, 1955.
- R. L. Roche. Modes of failures: Primary and secondary stresses. In *CEA conference 9098*, 1987.
- R. L. Roche. Practical procedure for stress classification. *International Journal of Pressure Vessels and Piping*, 37(14):27 – 44, 1989. ISSN 0308-0161. doi: [http://dx.doi.org/10.1016/0308-0161\(89\)90138-5](http://dx.doi.org/10.1016/0308-0161(89)90138-5). URL <http://www.sciencedirect.com/science/article/pii/0308016189901385>. Special Issue Design Codes and Structural Mechanics.
- C. E. Seow. Fracture testing cracked components with finite compliance applied displacements. Master's thesis, University of Bristol, England, 2015.
- C. Simsir and C. H. Gur. 3d {FEM} simulation of steel quenching and investigation of the effect of asymmetric geometry on residual stress distribution. *Journal of Materials Processing Technology*, 207(13):211 – 221, 2008. ISSN 0924-0136. doi: <http://dx.doi.org/10.1016/j.jmatprotec.2007.12.074>. URL <http://www.sciencedirect.com/science/article/pii/S0924013607014616>.
- D. J. Smith and S. Hadidi-Moud. Estimation of elastic follow-up in structures. In *Fracture and Strength of Solids VII*, volume 462 of *Key Engineering Materials*, pages 361–365. Trans Tech Publications, 4 2011.
- D. J. Smith, J. McFadden, S. Hadidi-moud, A. J. Smith, A. J. Stormonth-Darling, and A. A. Aziz. Elastic follow-up and relaxation of residual stresses. *Journal of Mechanical Engineering Science*, 2009.
- P. Withers and H. Bhadeshia. Residual stress. part 1 measurement techniques. *Materials Science and Technology*, 17(4):355–365, 2001. doi: 10.1179/026708301101509980. URL <http://www.tandfonline.com/doi/abs/10.1179/026708301101509980>.

A Appendices

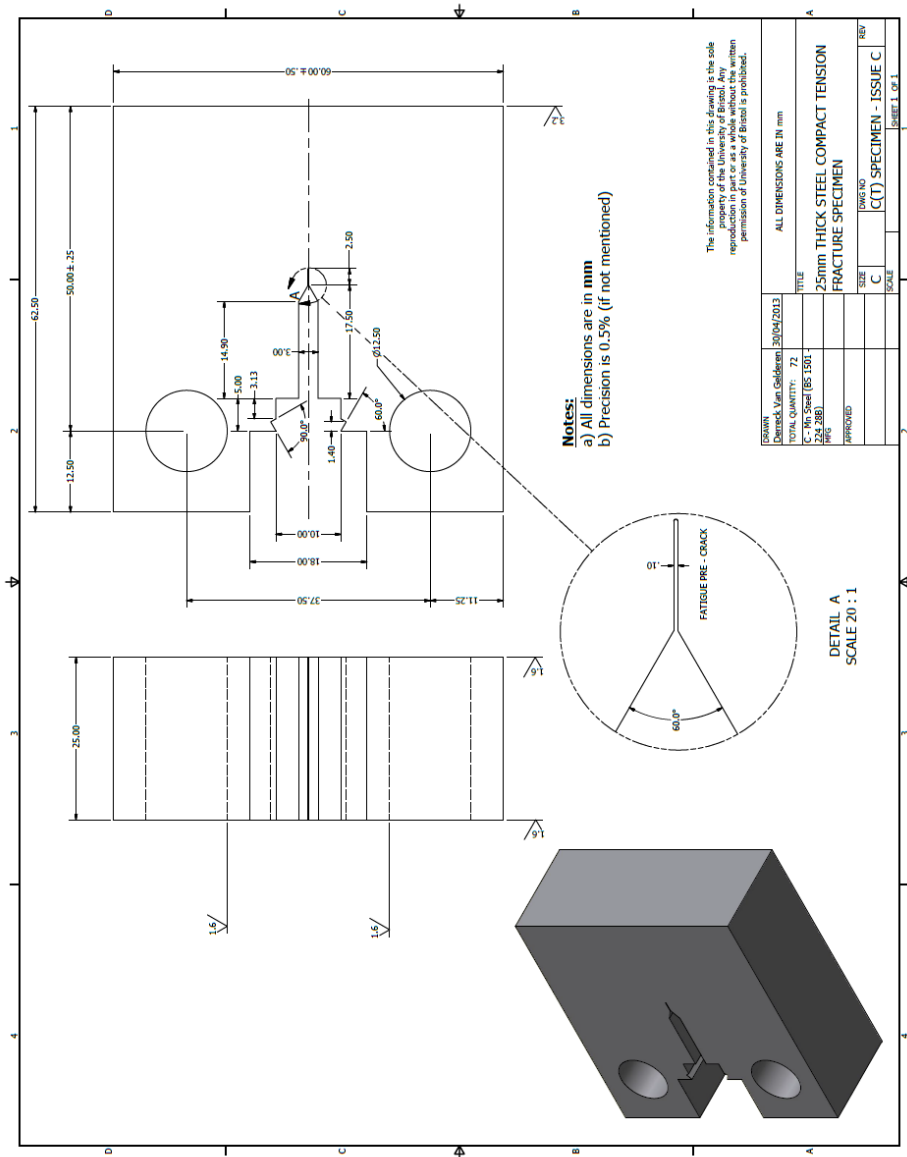
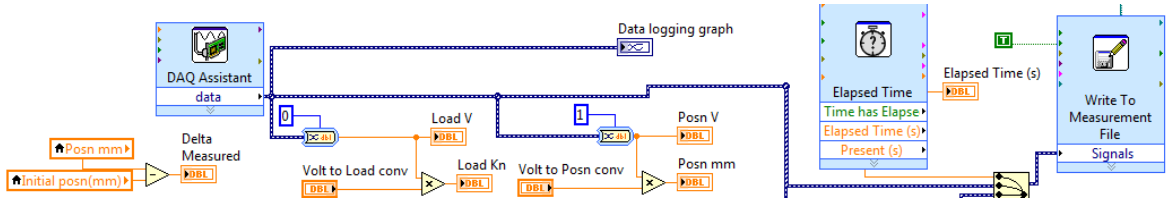
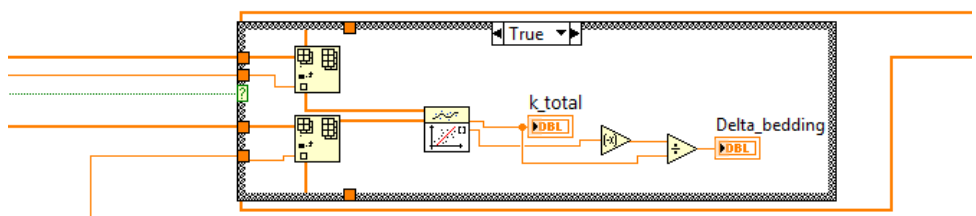


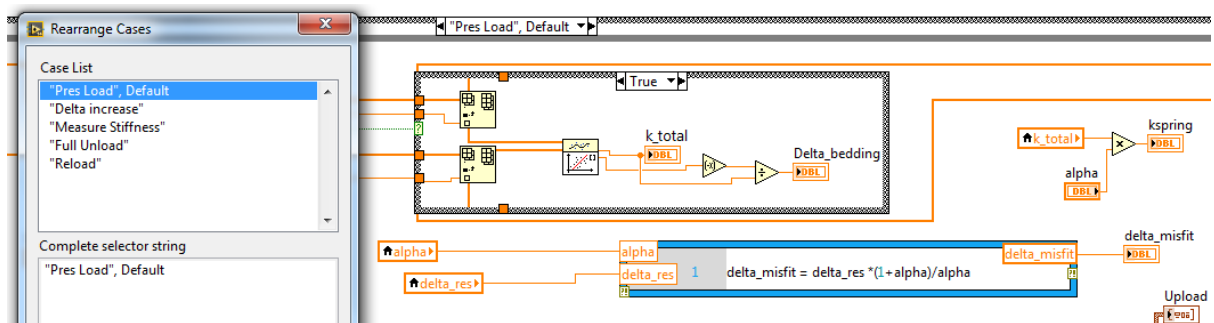
Figure A.1: CAD drawing of CT Specimen



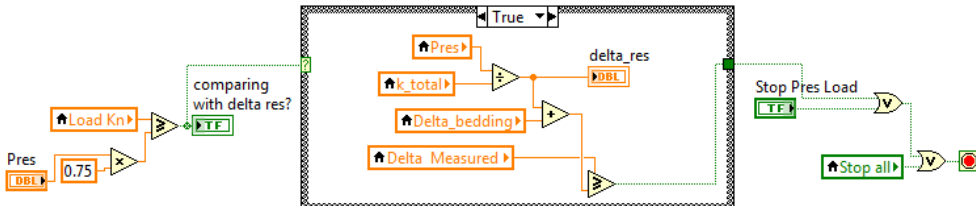
(a) Receiving data in DAQ Assistant and writing to measurement file



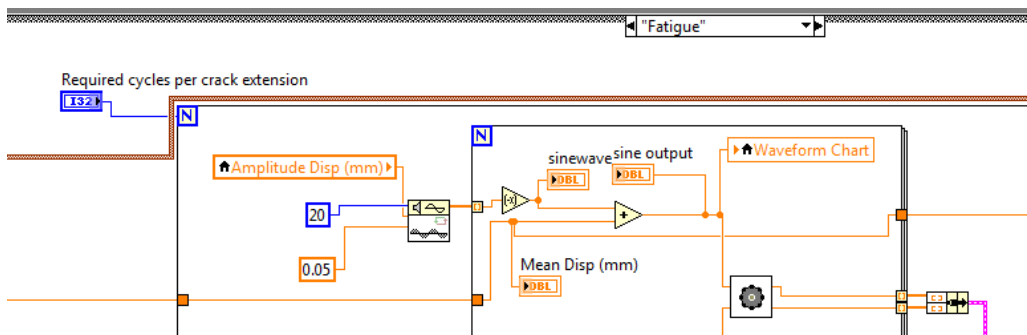
(b) Linear fit VI for stiffness measurement



(c) Case Structures used for sequential control



(d) Conditional terminal in while loop



(e) Sinewave generator VI used to set up fatigue cycles

Figure A.2: Snippets of LabVIEW controller code, (a) DAQ Assistant used to receive signals from the machine and Write to Measurement VI used for data logging. (b) Linear fit VI used to measure stiffness from measured load-displacement data, from which slope and intercepts can be found. (c) Case structures used to run the algorithm in specific sequence. (d) Conditional terminal used within the while loop for the initial load up to P_{res} . (e) Sinewave generator VI used to set up fatigue cycles, showing input amplitude, frequency and output signal, which was sent to the DAQ VI.